

MIT Open Access Articles

Atomic structure of the open SARS-CoV-2 E viroporin

The MIT Faculty has made this article openly available. **Please share** how this access benefits you. Your story matters.

Citation: João Medeiros-Silva et al. ,Atomic structure of the open SARS-CoV-2 E viroporin.Sci. Adv.9,eadi9007(2023).

As Published: 10.1126/sciadv.adi9007

Publisher: American Association for the Advancement of Science

Persistent URL: <https://hdl.handle.net/1721.1/153521>

Version: Final published version: final published article, as it appeared in a journal, conference proceedings, or other formally published context

Terms of use: Creative Commons Attribution





CORONAVIRUS

Atomic structure of the open SARS-CoV-2 E viroporin

João Medeiros-Silva, Aurelio J. Dregni, Noah H. Somberg, Pu Duan, Mei Hong*

The envelope (E) protein of the SARS-CoV-2 virus forms cation-conducting channels in the endoplasmic reticulum Golgi intermediate compartment (ERGIC) of infected cells. The calcium channel activity of E is associated with the inflammatory responses of COVID-19. Using solid-state NMR (ssNMR) spectroscopy, we have determined the open-state structure of E's transmembrane domain (ETM) in lipid bilayers. Compared to the closed state, open ETM has an expansive water-filled amino-terminal chamber capped by key glutamate and threonine residues, a loose phenylalanine aromatic belt in the middle, and a constricted polar carboxyl-terminal pore filled with an arginine and a threonine residue. This structure gives insights into how protons and calcium ions are selected by ETM and how they permeate across the hydrophobic gate of this viroporin.

INTRODUCTION

Coronaviruses have caused several epidemics and a global pandemic since the early 2000s (1–3), necessitating fundamental studies of the structure and function of the proteins of these viruses. The severe acute respiratory syndrome coronavirus 2 (SARS-CoV-2) virus encodes 29 proteins, 4 of which are structural: the spike protein (S), the nucleocapsid protein (N), the matrix protein (M), and the envelope protein (E) (4). The viral RNAs and proteins assemble in the endoplasmic reticulum Golgi intermediate compartment (ERGIC) of the cell (5). Here, the 75-residue E protein, conserved across SARS-CoV-2 variants, forms ion channels in the ERGIC membrane (6, 7). Cation conduction by the E protein is associated with the pathogenicity of the virus. E also mediates egress of the new virion (8, 9), senses membrane curvature (10, 11), and interacts with other viral and host proteins such as the human cell junction protein PALS1 and the immune receptor Toll-like receptor 2 (TLR2) (9, 12–15).

The transmembrane domain (TM) of E is chiefly responsible for the protein's ion channel activity. Electrophysiological data show that E's transmembrane domain (ETM) conducts K^+ , Na^+ , and Ca^{2+} in a pH-dependent manner (8, 16, 17). The calcium-conducting activity of E triggers the NLRP3 inflammasome (17), which leads to the acute respiratory symptoms that are associated with coronavirus disease 2019 (COVID-19). Impairment of the E channel activity in SARS-CoV-2 alleviates the inflammatory response and results in aberrant virion titers (16, 18). The ion channel activity of E may also prevent the premature activation of the spike protein for membrane fusion, by increasing the pH and leaking calcium of the ERGIC lumen (19, 20). In influenza viruses the analogous viroporin, M2, prevents premature cleavage of hemagglutinin by its proton channel activity (21). In the infectious bronchitis virus, the E protein similarly protects the spike protein from premature cleavage (22). These functions make the E protein of SARS-CoV-2 an antiviral drug target (16, 23).

The ETM amino acid sequence is identical between SARS-CoV and SARS-CoV-2. The conformation of ETM and longer constructs of E have been studied in detergent micelles using solution nuclear magnetic resonance (NMR), but with inconsistent results (24–26).

Recently, we determined the structure of ETM at neutral pH in lipid bilayers using solid-state NMR (27). The protein was reconstituted into an ERGIC-mimetic lipid membrane at neutral pH in the absence of calcium ions (28). The resulting structural model shows a tight helical bundle, suggesting that this structure reflects the closed state of the channel. ^{19}F spin diffusion NMR data provided direct evidence that the membrane-bound ETM is pentameric; moreover, the pentamers cluster in phosphatidylinositol (PI)-containing lipid bilayers (6). Despite these advances, how the E protein opens to conduct cations is not known.

Here, we use solid-state NMR to derive a high-resolution structural model of the open state of ETM, achieved under acidic pH in the presence of calcium ions. Electrophysiological data showed that the open probability of E increases at acidic pH (16, 17). Consistent with this, recent water-edited ssNMR data showed that ETM becomes more water-accessible at acidic pH and in the presence of calcium ions compared to the neutral-pH state (Fig. 1A) (29). By measuring a large number of distance and orientational restraints under the acidic and calcium-bound condition, we have obtained a 0.84-Å structure of the open state of ETM. This open state exhibits profound structural differences from the closed state, giving insights into the ion permeation mechanism of this hydrophobic SARS-CoV-2 viroporin.

RESULTS

Water accessibility of the ETM channel at acidic pH in the presence of calcium ions

We expressed isotopically labeled ETM in *Escherichia coli* and reconstituted it into both model membranes and an ERGIC-mimetic membrane (table S1) (30). The proteoliposomes were prepared in the presence of 30 mM Ca^{2+} at pH 4.5. These ionic conditions approximately reflect the higher concentration of calcium ions than proton in the ERGIC lumen, which has $\sim 100 \mu M Ca^{2+}$ and an acidic pH of 6 (31, 32).

Two-dimensional (2D) ^{13}C - ^{13}C , ^{15}N - ^{13}C , and ^{15}N - 1H correlation spectra of ETM at acidic pH in the presence of Ca^{2+} show similar chemical shifts as the protein at neutral pH (table S2 and fig. S1) (29). This indicates that the monomer conformation is little affected by the addition of protons and calcium. Similar to the closed state, the N- and C-terminal residues show increased dynamics compared to the central portion of the TM domain. To

Department of Chemistry, Massachusetts Institute of Technology, Cambridge, MA 02139, USA.

*Corresponding author. Email: meihong@mit.edu

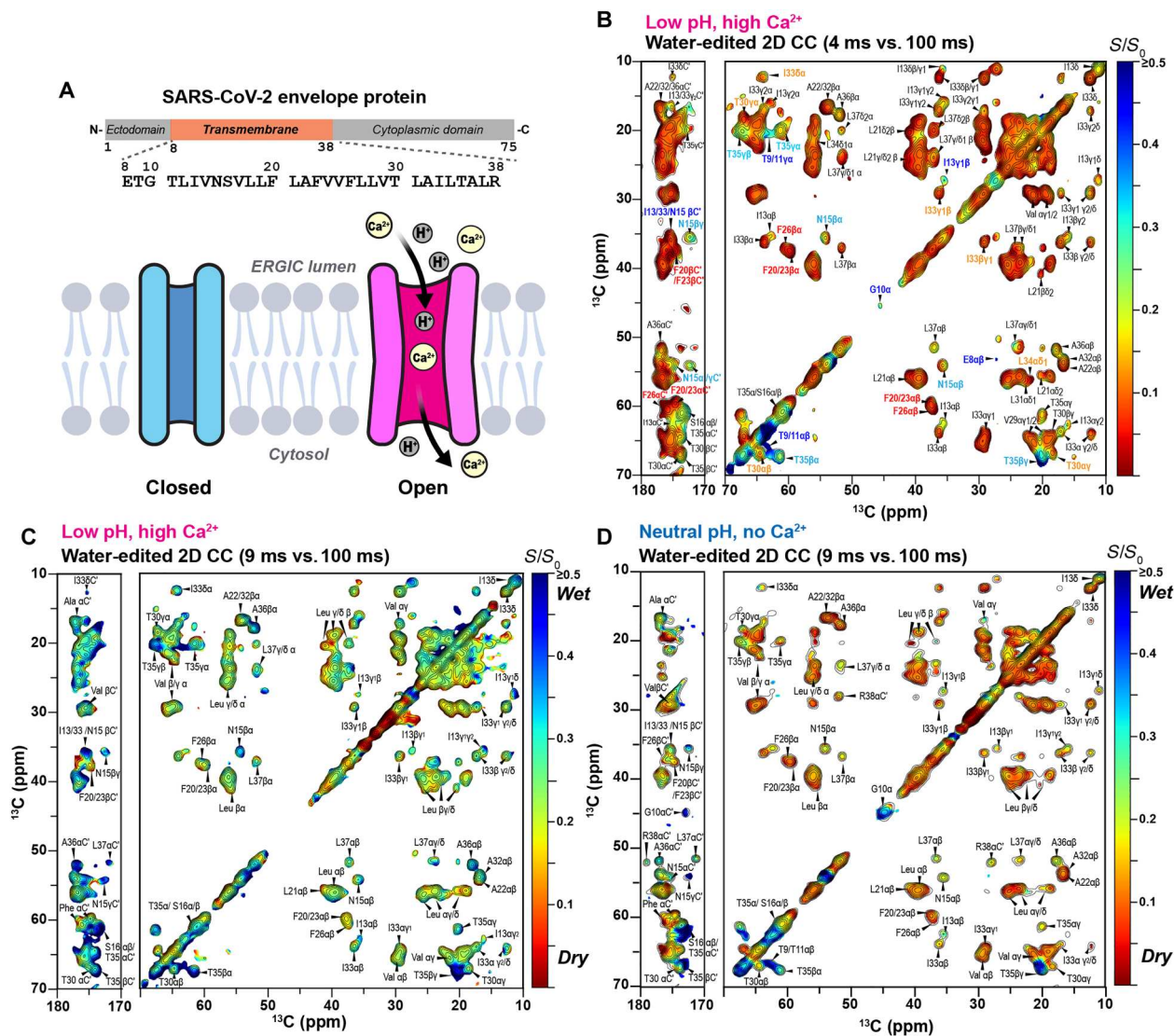


Fig. 1. Schematic model and experimental data of the opening of the SARS-CoV-2 E protein by low pH and Ca^{2+} ions. (A) Amino acid sequence of ETM and schematic model of its opening under acidic pH in the presence of Ca^{2+} ions. (B to D) Water-edited 2D ^{13}C - ^{13}C correlation spectra of membrane-bound ETM. The intensity ratios (S/S_0) between two spectra measured with short and long ^1H mixing times are shown in colored contours. (B) Water-edited spectra (4 ms versus 100 ms) of ETM at acidic pH in the presence of Ca^{2+} ions. The most water-accessible residues are assigned in blue and cyan. The three Phe residues have low water-transferred intensities and are assigned in red. C-terminal residues such as T30 and I33 are moderately hydrated and are assigned in orange. (C) Water-edited spectra (9 ms versus 100 ms) of ETM at acidic pH in the presence of Ca^{2+} ions. (D) Water-edited spectra (9 ms versus 100 ms) of the closed-state ETM at neutral pH (28). The neutral-pH ETM is much less water accessible than the low-pH ETM under the same experimental conditions.

verify that the proton- and calcium-rich condition opens the channel (Fig. 1A), we measured the water accessibility of the protein using water-edited 2D ^{13}C - ^{13}C correlation experiments (Fig. 1, B to D). This experiment transfers the water ^1H magnetization to the protein and detects it through ^{13}C signals. By comparing the intensities of spectra measured with a short ^1H mixing time of 4 or 9 ms to equilibrated spectra measured with 100-ms ^1H mixing, we obtain residue-specific water accessibilities. With 4 ms ^1H mixing, the 2D CC spectrum of the low-pH ETM shows heterogeneous hydration (Fig. 1B): The N-terminal residues E8 to I13 are highly water accessible, whereas the middle of the peptide from L19 to T30 are dehydrated. Residue N15, whose mutation abolishes

the channel conductivity (8, 33), shows moderate hydration, suggesting that this residue might not face the pore under this acidic and calcium-bound condition. Near the C terminus, residues T30 and I34 show lower water accessibility than the N-terminal residues, but T35 is well hydrated. Increasing the mixing time to 9 ms increased the intensities of all residues for the low-pH Ca^{2+} -bound sample (Fig. 1C), and these intensities exceed those of closed ETM at the same mixing time (Fig. 1D) (28). These results are confirmed by water-edited 2D ^{15}N - ^1H correlation spectra (fig. S2A). Together, these data indicate that protons and calcium induce a more spacious and more water-accessible channel pore compared to the neutral-pH ETM. Therefore, we denote the

protein at low pH with calcium as the open ETM, while the neutral-pH calcium-free protein is denoted as the closed ETM.

Orientation of the open ETM channels in lipid bilayers

To determine the structure of the open ETM, we first measured the helix orientation using motionally averaged ^{15}N - ^1H dipolar couplings. Under fast uniaxial rotation of the helical bundle, the motionally averaged ^{15}N - ^1H dipolar couplings reflect the orientation of the helix axis relative to the bilayer normal (34, 35). Previous solution NMR studies of the E protein in detergent micelles showed varying helix orientations depending on which detergent micelles were used and whether the TM peptide or longer constructs that contain the cytoplasmic segment were used (26, 36). The closed ETM structure that we recently solved did not contain orientation restraints because the protein was immobilized in the cholesterol-containing ERGIC-mimetic membrane (28). To enable fast uniaxial rotational diffusion, we reconstituted ETM into a low-viscosity 1-palmitoyl-2-oleoyl-*sn*-glycero-3-phosphocholine (POPC): 1-palmitoyl-2-oleoyl-*sn*-glycero-3-phosphoglycerol (POPG) membrane at pH 4.5 without Ca^{2+} (table S1) and measured the ^{15}N - ^1H dipolar couplings at 38°C. Comparison of the protein chemical shifts indicates that the temperature change from 10° to 38°C only affects the dynamics and not the conformation of most residues (fig. S3). At this elevated temperature, 2D ^{15}N - ^1H and ^{13}C - ^1H dipolar-shift correlation (DIPSHIFT) spectra show an average N-H order parameter (S_{NH}) of 0.90 and C-H order parameters (S_{CH}) of 0.6 to 0.8 (Fig. 2, A to D). The substantial reduction of S_{CH} from the rigid limit of 1.0 and the large S_{NH} value are characteristic of slightly tilted helices undergoing uniaxial rotational diffusion around the bilayer normal. To measure the ^{15}N - ^1H dipolar couplings site-specifically, we resolved them by 2D ^{15}N - ^{13}C correlation spectra (Fig. 2E). The ETM chemical shifts indicate an α helix for most of the residues (fig. S1B); thus, we fit the site-resolved S_{NH} values to α -helical periodicity. The resulting “dipolar wave” shows three orientational regimes for the open ETM (Fig. 2F and table S3): Residues E8 to L12 are dynamically disordered, residues I13 to L27 in the center of the protein have a small tilt angle of 5°, whereas residues T30 to L37 adopt a slightly larger tilt angle between 7° and 10°. Thus, the TM helix of the open ETM is nearly parallel to the channel axis, except for the C-terminal portion, which is more tilted. Alternative simulations using a single-tilt angle for the entire ETM resulted in poorer agreement with the experimental data (fig. S4). The C-terminal residues $^{35}\text{TAL}^{37}$ exhibit torsion angles that are more consistent with a 3_{10} helix rather than an α helix (fig. S1B) (37), suggesting that this polar segment of the channel has a slightly different conformation from the rest of the TM domain.

Interhelical packing of the open ETM channel

With the helix orientation determined, we next measured interhelical contacts within the open ETM. ^{19}F spin diffusion Centerband-Only Detection of Exchange (CODEX) data (6, 38) showed that the closed ETM forms a pentameric channel in lipid bilayers. To verify that the oligomeric state is unchanged under the acidic and Ca^{2+} -bound condition, we conducted the ^{19}F CODEX experiment using 4- ^{19}F -Phe23-labeled ETM at acidic pH in the presence of Ca^{2+} . Spin diffusion among n -monomers of an oligomeric protein should reduce the CODEX intensities to $1/n$. Figure S5 shows that the normalized ^{19}F CODEX intensities as a function of mixing time

equilibrate to ~ 0.20 , consistent with pentamer formation. Thus, ETM remains pentameric in the open state, unchanged from its oligomeric state at neutral pH.

To measure distance restraints, we carried out a variety of 2D correlation experiments (tables S4 to S7) using strategic isotopic labeling to distinguish interhelical from intrahelical distances (fig. S6A). Equimolar mixtures of two differently labeled proteins allowed the measurement of interhelical distances, whereas sparsely ^{13}C -labeled ETM diluted by ^{13}C natural abundance protein allowed us to obtain intrahelical distances.

2D ^{13}C - ^{13}C correlation spectra were measured using three mixed labeled samples to obtain distance restraints. A mixture of 1,3- ^{13}C -ETM and 2- ^{13}C -ETM (Fig. 3A) provided interhelical ^{13}C - ^{13}C contacts. 1,3- ^{13}C -glycerol preferentially labels C β and C' of most amino acid residues, whereas 2- ^{13}C -glycerol preferentially labels Ca (39, 40). Leucine residues, however, follow the opposite pattern. Using a ^{13}C spin diffusion mixing time of 300 ms, we observed numerous intermolecular correlations such as L19Ca-A22Ca, F20Ca-A22C β , and L31Ca-A32Ca (Fig. 3, A and B). These cross peaks are absent in a control spectrum of an equimolar mixture of 1,3- ^{13}C -ETM and ^{15}N -ETM, thus confirming their intermolecular nature. Because of the 50% ^{13}C dilution in the 1,3- ^{13}C and ^{15}N mixture, the spectrum of this sample (fig. S6B) also provided unambiguous intramolecular correlations such as I13C γ 1-N15Ca and L18/19Ca-S16C β . Last, we measured and compared the 2D CC spectra of U- ^{13}C , ^{15}N -labeled ETM with a 50% diluted sample containing a mixture of U- ^{13}C -ETM and ^{15}N -ETM (fig. S6, C and D). Cross peaks that are stronger in the U- ^{13}C , ^{15}N -ETM spectrum compared to the diluted sample spectrum contain contributions from intermolecular contacts (fig. S6D). We found intermolecular contacts between I13 side chains, between L31 residues, and between V29 and I33 residues, suggesting that many of these residues lie at the helix-helix interface.

A second type of intermolecular distance restraints was obtained between amide H $^{\text{N}}$ of one helix and carbons of another helix using the NHHC experiment (Fig. 3C). The ^{15}N -labeled ETM was fractionally deuterated to reduce the impact of intramolecular carbon-bonded ^1H on ^{15}N - ^{13}C correlations (41). The NHHC spectrum revealed numerous C-terminal interhelical contacts, including T35N-T35Ca, A32N/A36N-I33Ca, I33N/L34N-A32C β , and R38Ne-T35C γ . To confirm the chemical shift assignment, we also measured an NHHC spectrum of mixed 1,3- ^{13}C -ETM and ^{15}N -ETM (fig. S7). Spectral comparison confirmed the assignment of interhelical contacts between R38Ne on one helix and T35C γ and A36C β on another, and between R38C ζ and I33N/L34N (Fig. 3D). These correlations suggest that the R38 side chain points to neighboring helices rather than to lipids. In comparison, the closed ETM exhibits no interhelical contacts involving the R38 side chain (28). Together, these results indicate that although the C-terminal region of the open ETM is better hydrated than the closed ETM, it is more compact, with the R38 guanidinium side chain likely occupying the pore. At the same time, the center of the TM domain is more expanded in the open state compared to the closed state, as seen by weaker interhelical correlations for the three Phe residues (Fig. 3E) (28, 29).

To directly probe the conformation of the aromatic side chains and their neighboring residues, we conducted ^{13}C - ^{19}F rotational-echo double-resonance (REDOR) experiments. We used an equimolar mixture of ^{13}C , ^{15}N -labeled ETM (CN-ETM) and 4- ^{19}F -

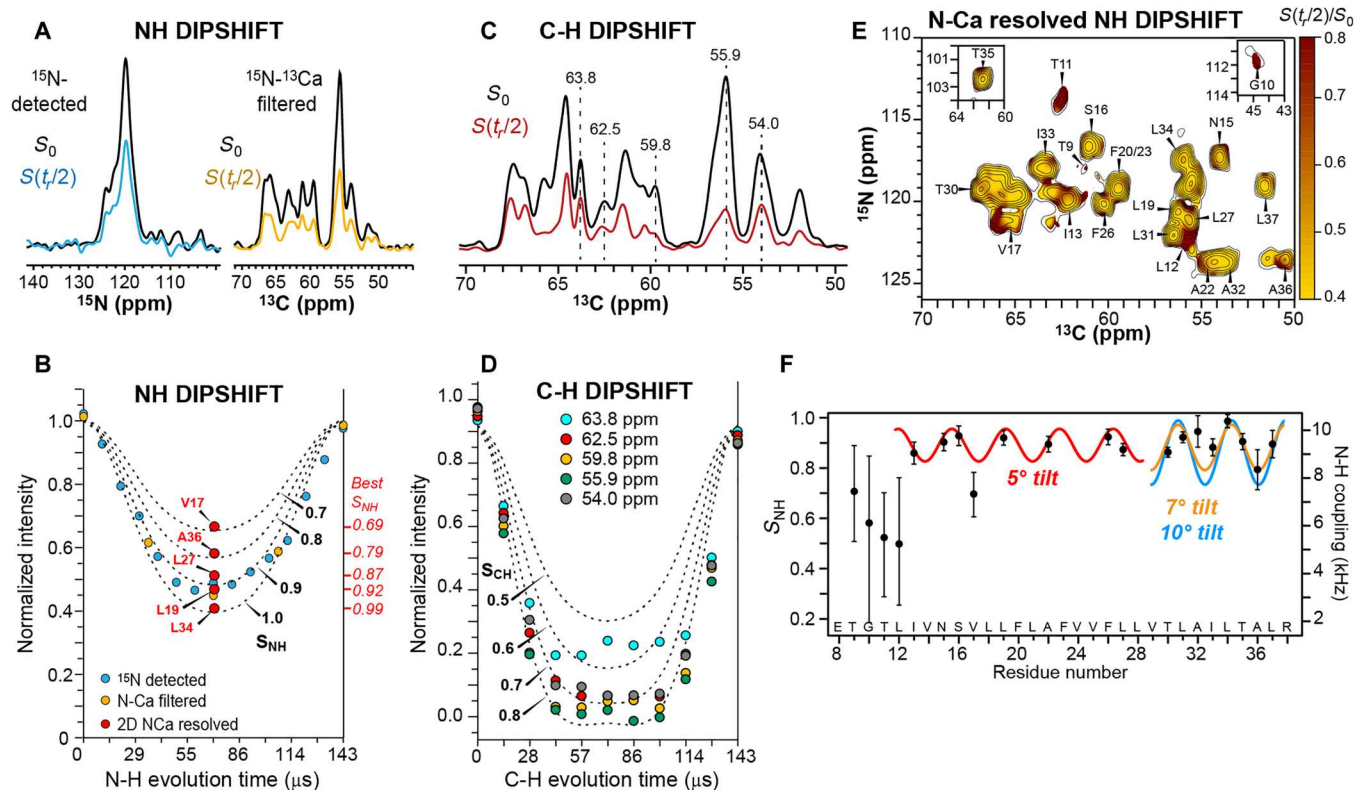


Fig. 2. Orientation of membrane-bound ETM helices at low pH in the presence of Ca^{2+} . (A) ^{15}N -detected (left) and ^{13}C -detected (right) ^{15}N - ^1H DIPSHIFT spectra, measured with zero N-H dipolar dephasing, S_0 , and half a rotor period of dephasing, $S(t/2)$. The ^{13}C -detected spectra (right) were measured with a ^{15}N - ^{13}C dipolar filter and indirectly encode the backbone N-H dipolar coupling. (B) N-H DIPSHIFT dephasing measured with ^{15}N detection (cyan circles) and ^{13}C detection after an N-C filter (yellow circles). The two data agree well and show an average S_{NH} value of ~ 0.90 . Dashed lines are simulated N-H DIPSHIFT curves for 7-kHz MAS. (C) C-H DIPSHIFT spectra measured with zero (S_0) and half a rotor period [$S(t/2)$] of C-H dipolar dephasing. (D) C-H dipolar dephasing (circles) of representative Ca peaks, overlaid with simulated DIPSHIFT curves (dashed lines). The measured S_{CH} values range from 0.6 to 0.9, confirming that the helical bundle undergoes fast uniaxial rotational diffusion. (E) 2D ^{15}N - ^{13}C resolved ^{15}N - ^1H DIPSHIFT spectra. Color contours show the intensity ratios $[S(t/2)/S_0]$ between a spectrum measured with half a rotor period of N-H dipolar dephasing and a spectrum without dipolar dephasing. (F) Site-resolved N-H dipolar couplings and S_{NH} values obtained from the 2D N-Ca-resolved N-H DIPSHIFT data. The couplings fit to a helix tilt angle of 5° for residues 13 to 27 and 7° to 10° for residues 30 to 37.

Phe²⁰-labeled ETM to measure exclusively interhelical distances. REDOR experiments report heteronuclear distances through dipolar-induced intensity decrease between a ^{13}C control spectrum measured without ^{19}F pulses (S_0) and a ^{13}C spectrum measured with ^{19}F pulses (S). Shorter distances cause faster dipolar dephasing, with lower S/S_0 values, which leads to high intensities in the difference spectrum, ΔS . Using REDOR mixing times of 2.3 to 10.3 ms, we observed ^{19}F dephasing of many ^{13}C signals such as V24/V25 and F20/F23 Ca (Fig. 4, A and B), indicating that these Ca carbons are in close contact with 4- ^{19}F -Phe²⁰ of the neighboring chain. These experiments were conducted in ETM reconstituted in the ERGIC-mimetic membrane at a high protein monomer/lipid molar ratio (P/L) of 1:9 to obtain sufficient sensitivity. Recent ^{19}F spin diffusion NMR data showed that ETM pentamers cluster in this ERGIC-mimetic membrane, but clustering was suppressed after the removal of PI (6). To assess whether the measured ^{13}C - ^{19}F REDOR dephasing has contributions from interchannel contacts, we repeated the ^{13}C - ^{19}F REDOR experiment in a PI-free membrane at a lower P/L of 1:22 (fig. S8). The REDOR spectra of this more dilute sample no longer exhibit Phe side-chain ^{13}C difference signals (fig. S8B), indicating that interhelical aromatic-aromatic

REDOR dephasing in the ERGIC-bound ETM at high P/L has contributions from interchannel contacts. For the diluted sample, we observed ^{19}F - ^{19}F cross peaks between the two Phe²⁰ conformations in 2D ^{19}F - ^{19}F correlation spectra (fig. S8C). This indicates that the two Phe²⁰ side-chain conformations occur within each pentamer, separated by less than ~ 2 nm. This distance range is detectable by ^{19}F spin diffusion (42) but longer than the upper bound of measurable ^{13}C - ^{19}F REDOR distances (43).

To further complement the ^{13}C - ^{19}F distance restraints, we measured interhelical ^1H - ^{19}F distances using a ^1H -detected ^1H - ^{19}F REDOR experiment (43, 44). A ^2H , ^{13}C , ^{15}N -labeled ETM sample (CDN-ETM) was mixed with 4- ^{19}F -Phe²⁰ ETM for this purpose. CDN-ETM yielded well-resolved 2D hNH spectra under 55-kHz magic-angle spinning (MAS) (Fig. 4C). The ^1H and ^{15}N chemical shifts were readily assigned using 3D hCANH and hCA(CO)NH spectra (fig. S9). With 3.4-ms ^1H - ^{19}F REDOR mixing (Fig. 4D), we observed difference intensities for the ^1H protons of residues L21 to T30 (Fig. 4E), but no residues N-terminal to this region. Notably, V29 and T30 are dephased by 4- ^{19}F -Phe²⁰, suggesting that the F20 side chain points to the C terminus. The ^1H - ^{19}F measurements were performed at a low P/L of 1:30 to minimize the

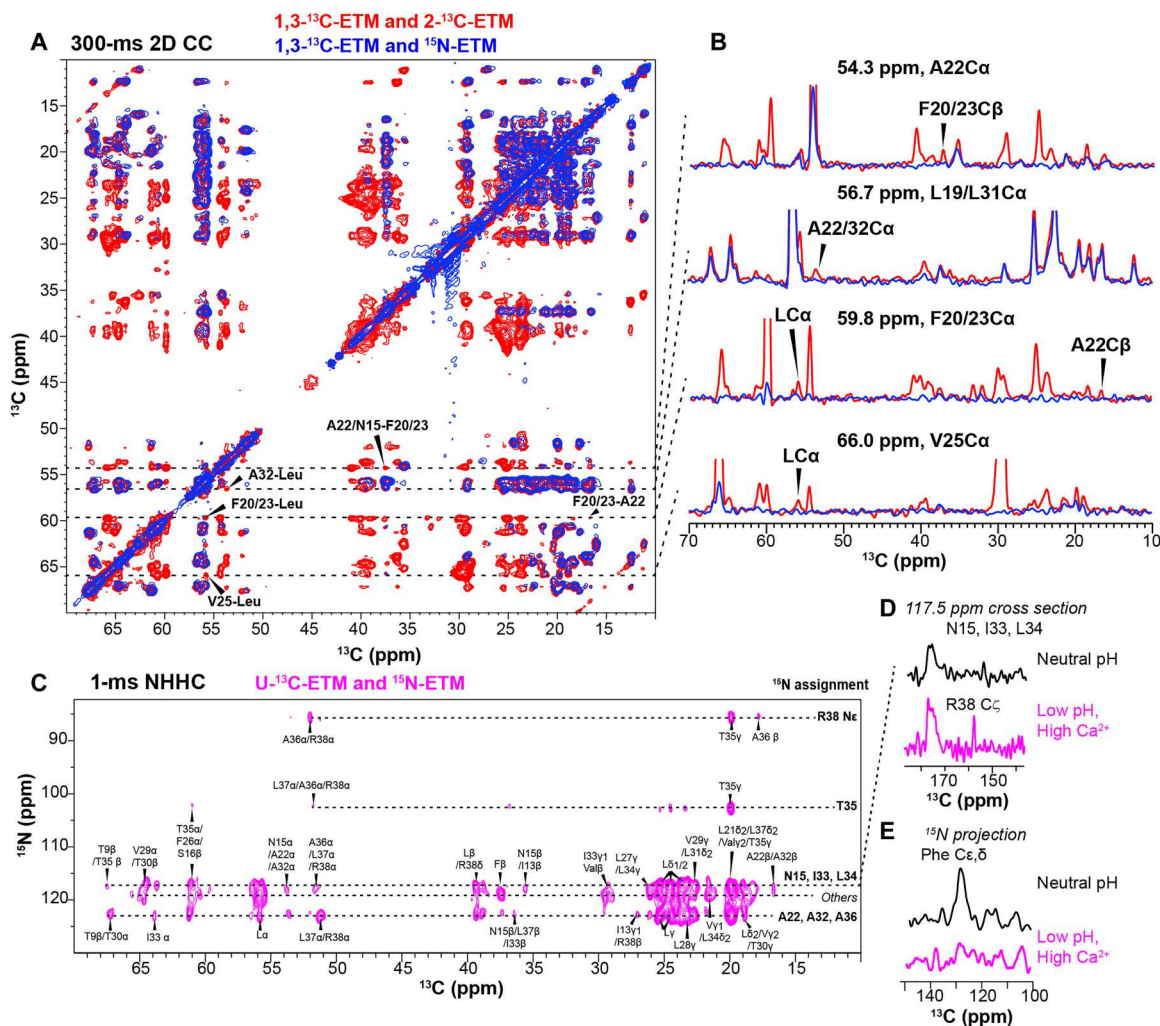


Fig. 3. Interhelical ^{13}C - ^{13}C and ^{13}C - ^{15}N distance restraints from mixed labeled ETM samples. (A) 2D CC spectrum (300 ms) of mixed 1,3- ^{13}C -ETM and 2- ^{13}C -ETM (red). This is overlaid with a control spectrum of 1,3- ^{13}C -ETM diluted by ^{15}N -labeled ETM (blue). Additional cross peaks in the mixed 1,3- and 2- ^{13}C -labeled sample compared to each sample alone represent interhelical contacts. (B) Representative 1D cross sections from the indicated ω_1 chemical shifts. The assigned peaks can only arise from interhelical contacts. The two spectra were normalized by matching the 50% diluted sample's intensity with the 1,3- and 2- ^{13}C -labeled sample intensity for the resolved L37 Ca cross section (51.7 ppm) and the I13 Cy1 cross section (16.0 ppm). (C) 2D NHHc spectrum of mixed U- ^{13}C -ETM and ^{15}N -ETM measured with 1-ms ^1H mixing. The ^{13}C assignments are indicated at the specific peaks, while ^{15}N assignments are given on the right for ^{15}N cross sections. All observed correlations are interhelical. (D) 1D ^{15}N cross section at 117.5 ppm for I33N or L34N. A cross peak with R38 guanidinium is seen in the low-pH spectrum but not in the neutral-pH spectrum, indicating that R38 forms close contact with I33/L34 of the neighboring helix in the open state. (E) 1D ^{13}C projections of the 2D NHHc spectra of ETM at neutral pH and low pH. The low-pH sample shows weaker aromatic cross peaks.

effects of interchannel contacts, which are seen at higher P/L ratios (fig. S10).

Structure of the open ETM in lipid bilayers

Combining the chemical shift-derived (ϕ and ψ) torsion angles, DIPSHIFT-derived N-H bond orientations, and intramolecular and intermolecular distance restraints, we calculated the structural model of the open ETM (Table 1 and table S8) (45). The protein is modeled as a C5-symmetric pentamer except for residues F20 and F26, which show two side-chain conformations (29). The lowest-energy ensemble of 30 structures has a heavy-atom root mean square deviation (RMSD) of 0.84 Å and shows five right-handed helices whose N-terminal two-thirds surround a spacious pore (Fig. 5A). This wide N-terminal pore of the open state differs

substantially from the pinched N-terminal pore of the closed channel (Fig. 5C). The mouth of the open ETM is lined by a disordered E8, while the C-terminal end is marked by a disordered and pore-facing R38. The TM helix is slightly kinked at residues $^{19}\text{LFLA}^{22}$, consistent with the C β chemical shifts (fig. S1A). The C-terminal third of the TM helix from residue T30 tilts toward the channel axis, narrowing the pore, giving a conical shape to the helical bundle. Moreover, this more tilted segment forms an unexpected 3_{10} helix, with i to $i + 3$ hydrogen bonds for residues between L31 and L37 (Fig. 5B). The pore is the most constricted at L28 (Fig. 5D), followed by T35, before it widens toward the C-terminal side of the membrane surface.

The side chains of the open ETM structure are well defined (Fig. 5E and fig. S11). The water-filled pore is almost entirely

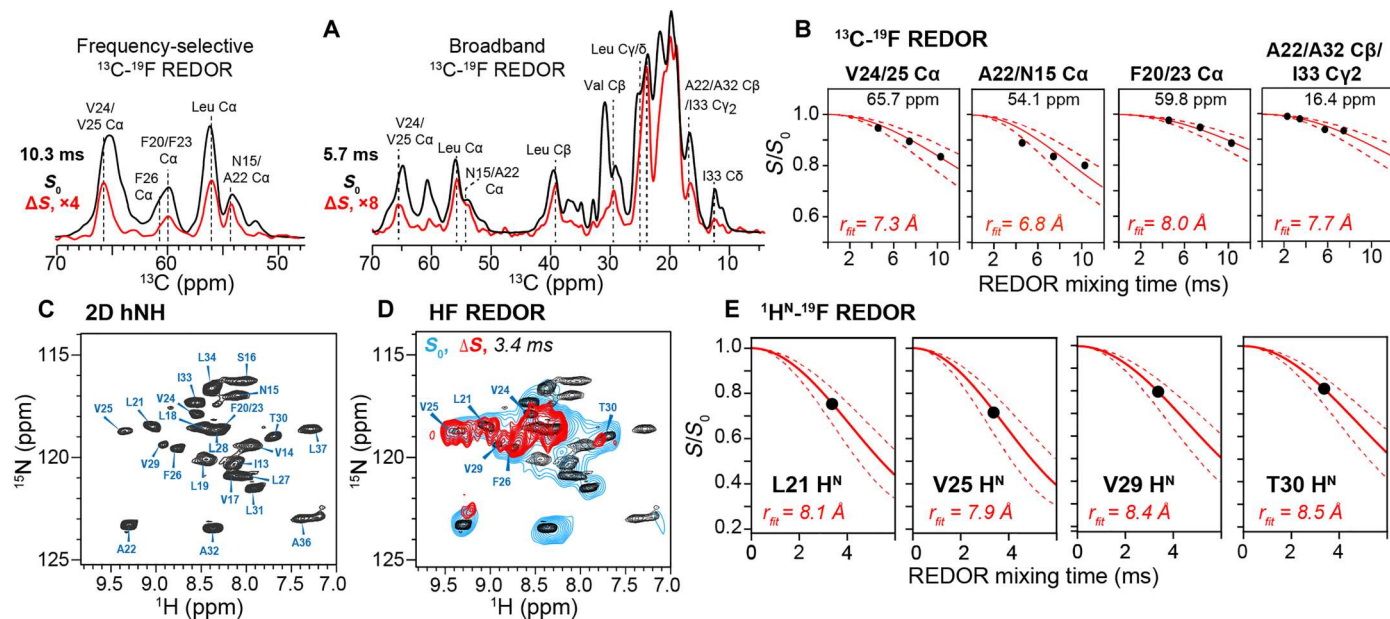


Fig. 4. Interhelical distance measurements using ^{13}C - ^{19}F and ^1H - ^{19}F REDOR experiments. $4\text{-}^{19}\text{F}$ -Phe 20 -labeled ETM is mixed with ^{13}C , ^{15}N -labeled ETM or ^{13}C , ^2H , ^{15}N -labeled ETM and bound to lipid membranes at pH 4.5 in the presence of Ca^{2+} . (A) Representative ^{13}C - ^{19}F REDOR S_0 and ΔS spectra, measured in a Ca frequency-selective manner (left) and broadband manner (right). The spectra were measured under 14-kHz MAS at 287 K, and the sample has a P/L ratio of 1:9 in the ERGIC membrane. (B) Representative ^{13}C - ^{19}F REDOR dephasing curves for resolved sites. Best-fit simulations are shown as solid lines, while simulations for distances that are ± 0.5 Å from the best-fit values are shown as dashed lines to give approximate uncertainties. Simulations take into account ^{19}F CSA, ^{19}F pulse imperfections, and the sample dilution factor of 50%. (C) 2D hNH spectrum of CDN-labeled ETM measured under 55-kHz MAS. Resonance assignment obtained from 3D spectra is shown. (D) 2D hNH-resolved ^1H - ^{19}F REDOR S_0 (cyan) and ΔS (red) spectra of CDN-labeled ETM mixed with 4F-Phe 20 -ETM at a total P/L of 1:30. The protein is reconstituted in a DMPC- d_{54} :DMPG- d_{54} membrane. These REDOR spectra were measured under 38-kHz MAS with a mixing time of 3.4 ms. The 55-kHz spinning 2D hNH spectrum in (C) is overlaid for comparison. (E) Representative ^1H - ^{19}F REDOR dephasing of resolved H^{N} signals. Best-fit simulations (solid lines) and simulations for distances that are ± 0.5 Å from the best-fit values (dashed lines) give the interhelical distances and their uncertainties.

lined by hydrophobic Leu and Val residues (Fig. 5F), punctuated only by a polar T35 near the C terminus. The other polar residues of the protein either lie at the helix-helix interface, such as T11 and S16 (Fig. 5G), or face lipids, such as N15 and T30 (Fig. 5H). These spatial distributions are consistent with the water-edited 2D spectra (Fig. 1B), which show that T35 is well hydrated, T30 is relatively dry, whereas N15 is moderately hydrated despite its location in the N-terminal water chamber. The lipid-facing position of N15 is further confirmed by lipid-edited 2D spectra (fig. S2B), which show high ^1H magnetization transfer from lipid chains to N15. Lipid magnetization transfer is also seen for residues such as I13, L31, and T30. The helix packing is stabilized by methyl interdigitation between Leu, Val, and Ile residues (Fig. 5G and fig. S11C). The narrowest point of the pore occurs at L28, whose van der Waals pore diameter is ~ 3.4 Å (Fig. 5, D and F), which is barely large enough to pass a water molecule (46). F20 and F26 side chains point to lipids (Fig. 5H), mainly sampling the gauche minus and trans conformations. These orientations differ from the interfacial positions of these aromatic residues in the closed channel (28). Thus, Phe residues in the open ETM do not block the channel pore.

DISCUSSION

Similarities and differences between the open and closed ETM structures

One of the functions of the SARS-CoV-2 E protein is cation conduction from the ERGIC lumen to the cytoplasm in virus-infected host cells. The ERGIC compartment is acidic (47, 48) and has 1000-fold higher calcium concentration than the cytoplasm (31, 32). pH-sensitive cation conduction by E is implicated in the activation of the NLRP3 inflammasome and the cytokine secretion after virus infection (16, 17). Therefore, determining the structure of ETM under the acidic and calcium-present condition is important for understanding the mechanism of action of this essential SARS-CoV-2 protein.

Our recent study showed that ETM forms a tight and cylindrical helical bundle at pH 7.5 in the absence of calcium (28). The helical bundle is pentameric, as shown by ^{19}F spin diffusion NMR data (6) and consistent with gel electrophoresis and sedimentation equilibrium data (49, 50). Here, we reconstituted ETM into ERGIC-mimetic membranes at pH 4.5 in the presence of calcium ions. Under this condition, ETM retains its pentameric state based on the ^{19}F CODEX data (fig. S5). Moreover, structure calculations assuming a C6 symmetry led to severely distorted helical bundles, whereas calculations assuming a C4 symmetry led to narrow TM pores that are inconsistent with the water-edited NMR data. Thus, apart from the ^{19}F CODEX data, the distance and orientational restraints support the pentamer nature of the open ETM. Backbone

Table 1. NMR and structure refinement statistics of SARS-CoV-2 ETM at acidic pH in the presence of Ca²⁺. Pairwise RMSD was calculated as the average RMSD between the lowest-energy structure and the other 29 structures in the lowest-energy ensemble.

NMR distance and angular constraints

Distance restraints	
Intramolecular long range ($ i - j \geq 5$)	6 × 5
Intermolecular	50 × 5
Dihedral-angle restraints	
φ	29 × 5
ψ	29 × 5
Total orientational restraints	
¹⁵ N- ¹ H dipolar couplings	16 × 5

Structure statistics

Violations (mean ± SD)	
Distance restraints (Å)	0.16 ± 0.020
Orientalional restraints (kHz)	0.57 ± 0.063
Dihedral-angle restraints (°)	1.06 ± 0.140
Maximum dihedral-angle violation (°)	11.98
Maximum distance-restraint violation (Å)	2.26
Maximum orientational-restraint violation (kHz)	2.76
Deviations from idealized geometry	
Bond lengths (Å)	0.005 ± 0.000
Bond angles (°)	0.506 ± 0.019
Improper (°)	0.318 ± 0.015
Average pairwise RMSD (Å)	
Heavy	0.84 ± 0.50
Backbone	0.67 ± 0.41

N-H bond orientational restraints and numerous intramolecular and intermolecular distance restraints indicate that the protein assembles into an α -helical barrel (51) with an inverted cone shape: The N-terminal two-thirds of the pore is spacious, whereas the C-terminal third is tight (Fig. 5). Compared to the closed state, the open ETM shows the largest pore expansion between residues G10 and F26 (Fig. 5D). In contrast, C-terminal to L28, the pore diameter profile reverses: The low-pH pore becomes more constricted than the neutral-pH pore. Therefore, the conformational change of ETM from the closed to the open state resembles alternating access of membrane transporters: The neutral-pH state is more open to the C-terminal cytoplasm, whereas the low-pH and Ca²⁺ bound state is more open to the N-terminal ERGIC lumen. This suggests that the open state of E is optimized for proton and calcium binding and permeation. The influenza A M2 proton channel also undergoes a transporter-like conformational change but in the reverse direction: The AM2 pore is spacious on the N-terminal side at neutral pH and converts to an inward-open conformation at acidic pH (52–54).

The N-terminal polar network may be the selectivity filter of ETM

The structure of the N-terminal entrance of the open ETM strongly suggests that the key cation-binding residue is E8 (Fig. 6, A to C). In the lowest-energy ensemble, about half of the structural models point the E8 side-chain carboxylate of one helix toward the T9 hydroxy group of the neighboring helix. The average separation between the carbonyl oxygen and the hydroxy oxygen is about 5.3 Å (Fig. 6B), which is sufficiently large to accommodate a partially dehydrated calcium ion (55, 56). Most of the remaining structural models point the E8 carboxyl group toward the aqueous solution, ready to accept protons (Fig. 6C). This structural distribution suggests that the dynamic conformation and interactions of E8 and T9 might regulate proton and calcium binding and release. The T9I mutant of E in the Omicron variant of SARS-CoV-2 is pH insensitive and has weaker cation selectivity (57), lending support to this mechanistic model. Below E8 and T9, residues T11, N15, and S16 provide a constellation of backbone and side-chain oxygen atoms with short O-O distances (Fig. 6A), which might further mediate proton and calcium permeation. Although the ETM construct does not include E7, in the full-length protein, this residue could also participate in this N-terminal selectivity filter.

This E8-centric calcium and proton selectivity model of ETM is consistent with the structures and functions of many calcium channels and proton-dependent membrane transporters. Negatively charged carboxylate side chains of Glu and Asp residues are key to calcium coordination (55, 56, 58, 59). In the calcium channel Orai, a ring of E178 side chains acts as the selectivity filter. Mutation of this Glu to Asp increased the channel permeability to monovalent cations (58). In the calcium channel TRPV6, a ring of D541 residues and a ring of T538 residues form two Ca²⁺ binding sites. The degree of interhelical separation of these side chains and the coupled Ca²⁺ occupancy at these two sites have been suggested to distinguish selective channels from nonselective channels in the TRP family (55). In a voltage-gated Ca_v channel, two Asp and Glu residues form high-affinity calcium-binding sites (59). Glu residues can also act as proton-binding sites in membrane proteins such as the multidrug resistance transporter EmrE (44, 60) and the CLC chloride/proton exchange transporter (61). When the E protein resides in the host cell ERGIC membrane, the N terminus of the TM domain faces the acidic and calcium-rich ERGIC lumen; thus, both protons and calcium ions can bind E8. Depending on the relative proton and calcium dissociation constants of E8, the ETM pentamers will have a distribution of charge states and a distribution of proton-bound versus calcium-bound E8. At neutral pH, more E8 residues will be unprotonated and hence available to coordinate calcium. As pH decreases, proton binding to E8 will compete with calcium binding, thus potentially destabilizing the bound calcium, allowing it to be released into the channel pore (58, 62).

The hydrophobic gate and the C-terminal polar network of ETM

After the N-terminal polar network, the middle segment of ETM from L18 to L34 is entirely hydrophobic, and the pore diameter decreases to a minimum of ~3.4 Å at L28. Extensive hydrophobic surfaces in constricted regions of channel pores have been found to dewet ion channels to form hydrophobic gates that impede ion passage (63–65). How protons and calcium can pass this L28 hydrophobic gate to traverse the entire pore is therefore important to

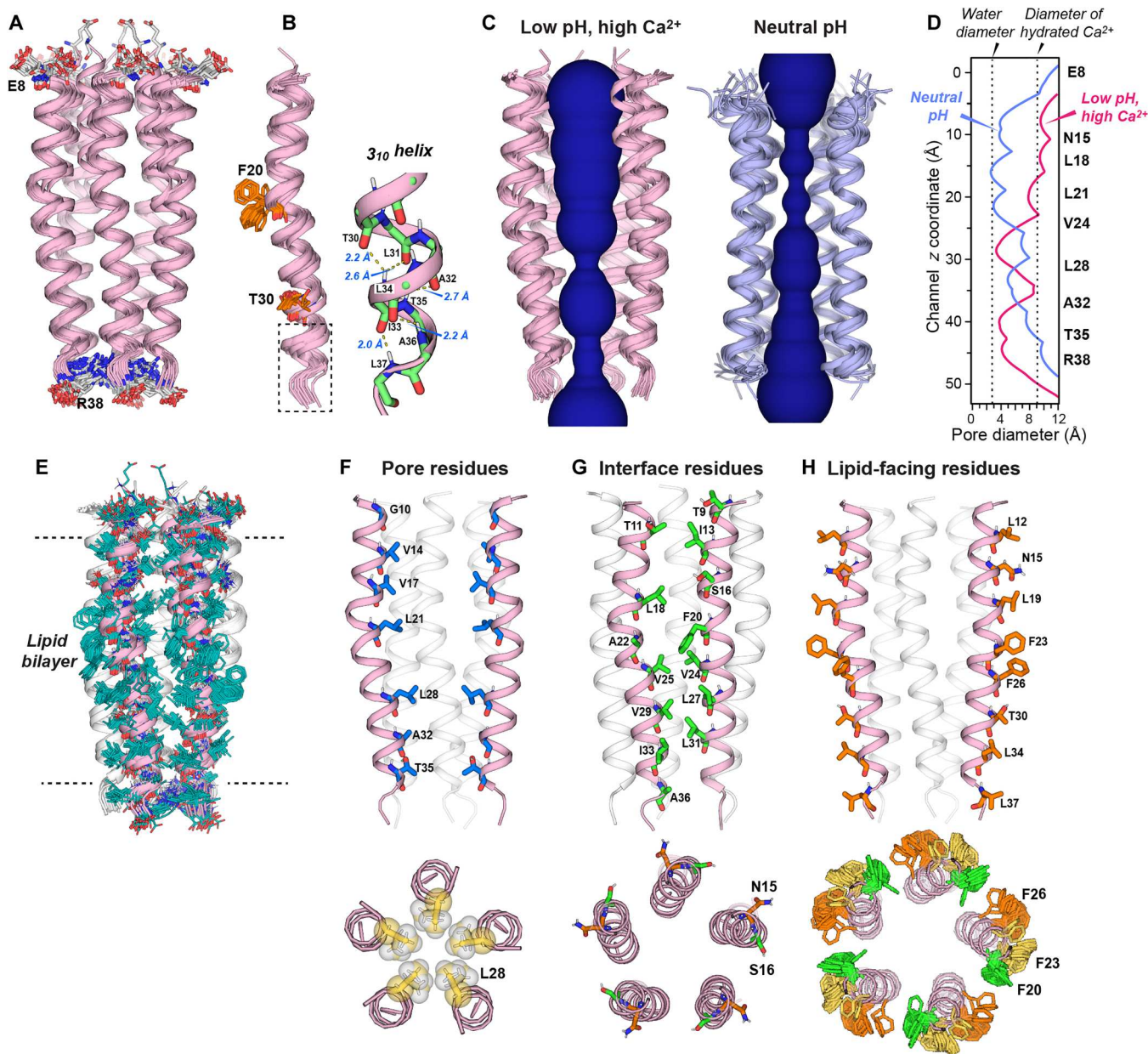


Fig. 5. Structure of membrane-bound ETM at acidic pH in the presence of Ca^{2+} . (A) Ensemble of 30 lowest-energy structure models. E8 and R38 cap the N and C termini, respectively. (B) The TM helix is slightly kinked near F20, and residues L31 to L37 form a 3_{10} helix with i to $i + 3$ CO-H^N hydrogen bonds. (C) HOLE plots of the pore diameters (dark blue) of the open (left) and closed (right) ETM channels. (D) Comparison of the pore diameters of the open and closed ETM along the channel coordinate z . The diameters of water and hydrated Ca^{2+} ions are indicated with dashed lines. (E) Structure ensemble showing the side chains of all residues in two neighboring helices. F20, F23, and F26 side chains are allowed to vary within a pentamer to adopt two rotamer conformations. The other three helices are shown in gray cartoons without side chains for clarity. (F) Pore-facing residues of the opposing helices i and $i + 2$ in the lowest-energy structure model (#1). N-terminal view at the bottom shows residue L28 with the van der Waals spheres. For clarity, the backbone ribbon starts from residue 27. (G) Helix-helix interface residues of two neighboring helices. N-terminal view shows the orientations of N15 and S16 in model #1. (H) Lipid-facing residues of two opposing helices i and $i + 2$. N-terminal view shows the positions and orientations of the three Phe residues in the ensemble. Each Phe residue adopts approximately two rotameric conformations.

address. We hypothesize that the C-terminal structure of the open ETM may be the key to unlock this hydrophobic gate (Fig. 6, D and E). These C-terminal residues $^{35}\text{TALR}^{38}$ form a second polar network that mirrors the N-terminal network: The R38 guanidinium protrudes into the pore, interacting with T35 and A36 of the neighboring helix. This polar network, together with the 3_{10}

helical backbone, tightens the C-terminal pore and increases its surface hydrophilicity. We speculate that this increased hydrophilicity might lower the free energy barrier for water and cation permeation through the L28 hydrophobic gate. Mechanistic models of polar side-chain conformational changes to open hydrophobic gates have been proposed for BK (66) and TRPV1 channels (67).

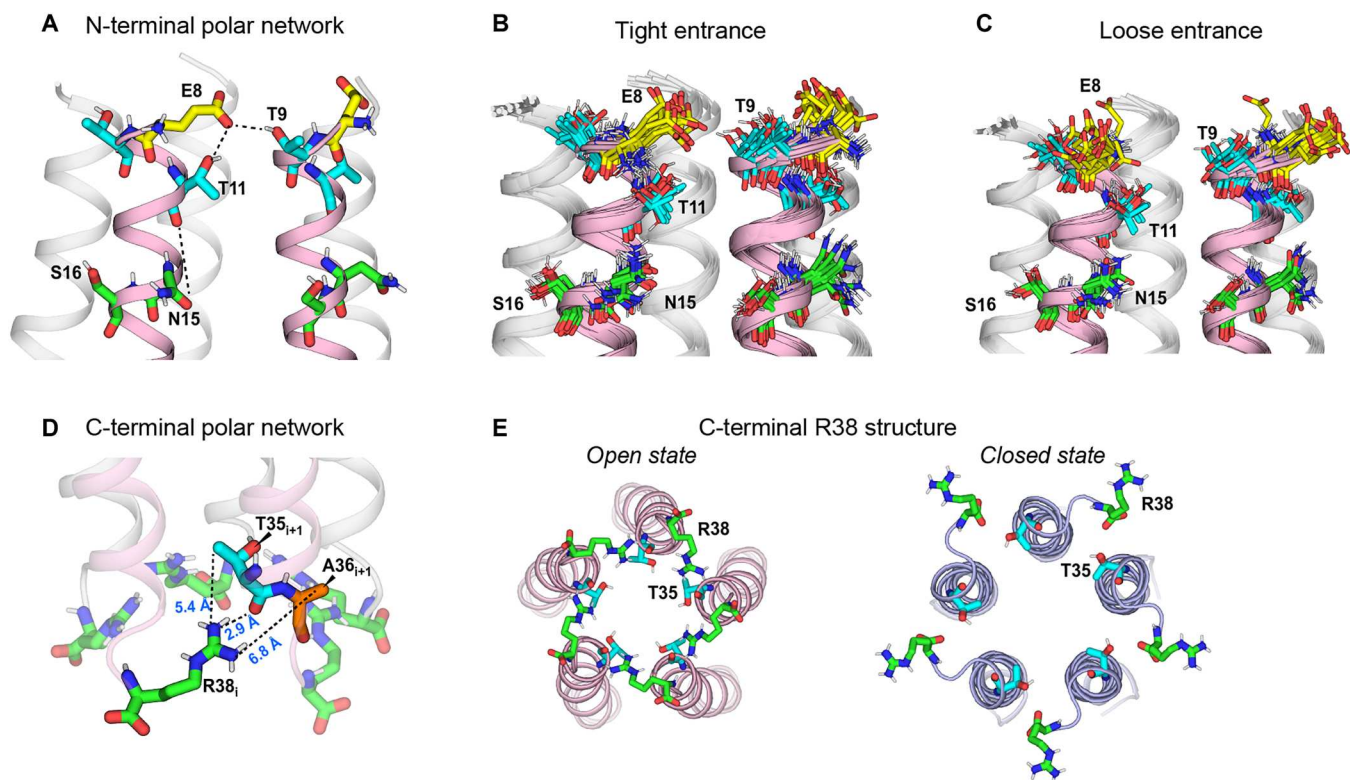


Fig. 6. N-terminal and C-terminal segments of the open ETM form two polar networks that may mediate cation selectivity and gating, respectively. (A) Lowest-energy structural model, showing key polar residues in the N-terminal region and their side-chain and backbone carboxyl and carbonyl groups. These functional groups may mediate calcium and proton binding. (B) Subset of the lowest-energy structural ensemble that shows close approach of E8 and T9 between two neighboring helices to potentially coordinate calcium. (C) Subset of the lowest-energy structural ensemble that shows the E8 side-chain carboxyl group pointing to the aqueous solution, ready for proton binding. Interconversion between these two populations is consistent with the weak intensities of N-terminal residues in the dipolar NMR spectra. (D) Side view of the C-terminal polar network of the open ETM. The R38 side chain protrudes into the pore, in close contact with the T35 side chain and A36 backbone of the neighboring helix. (E) Bottom views of the C-terminal region of the open (left) and closed (right) ETM. R38 side chain points to lipids in the closed state.

The pore-facing conformation of R38 in the open ETM differs markedly from its lipid-facing structure in the closed state (Fig. 6E) (28), suggesting that this R38 conformational change may be crucial for water and ion permeation through the hydrophobic gate. In designed membrane channels, the addition of a single polar residue to a hydrophobic pore has been shown to be sufficient to induce transient water wires (51, 68, 69). In full-length E, the cytoplasmic residues that immediately follow R38 form a flexible loop (11), suggesting that R38 may be able to execute these conformational changes in the full-length protein as well.

How do the two polar networks at the N and C termini communicate their conformational changes for ion permeation? We hypothesize that the triple-Phe motif between residues 20 and 26 may relay the signals of the two termini by regulating the aromatic side-chain conformations (Fig. 5H). Recent ^{19}F NMR data (29) showed that F20 and F26 each adopt two side-chain conformations that differ in their lipid and water exposures. Acidic pH and calcium increased the lipid-facing population and weakened interhelical contacts between these Phe residues. These results indicate that the conformational equilibria of F20 and F26 may regulate the channel pore diameter and the structural stability of the helical bundle (fig. S11B). An identical $^{530}\text{FxxFxxF}^{536}$ motif also exists in the calcium-selective TRPV6 channel and occurs at a similar distance from its own selectivity-filter residue D541 (56) compared

to the distance of F20 to E8 in ETM. Studies of designed TM helical bundles showed that placing aromatic residues at the *g* position of heptad repeats is prone to destabilize helix-helix packing (70, 71). In the open ETM structural models, L21 faces the pore, which puts F20 at the helix-helix interface near the *g* position. These observations suggest that the stability of the ETM helical bundle and the precise diameter of the pore at the hydrophobic gate may be tuned by the conformational equilibria of the three Phe residues. Increasing water diffusion through this central aromatic-rich region of the channel, as seen in the water-edited NMR spectra of the low-pH calcium-bound ETM, may induce R38 conformational changes, which in turn may lower the free energy barrier for cation permeation past the L28 hydrophobic gate to reach the C terminus.

The open ETM structure shown here is determined at protein/lipid molar ratios of 1:10 to 1:40. The concentration of E in the cell membrane is not known and may be lower. Our recent ^{19}F spin diffusion data (6) showed that the E pentamers cluster in lipid membranes containing PI, a key signaling lipid that interacts with and regulates membrane proteins (72). Therefore, E may also cluster in the PI-containing ERGIC membrane of the cell to increase its local concentration. Therefore, the structure of the open ETM determined here should shed light on the activation of the E channels in the ERGIC membrane of SARS-CoV-2-infected cells. Last, both the closed and open ETM channels have small helix tilt angles. This

would normally suggest membrane thickening to reduce the hydrophobic mismatch. However, the propensity for ETM channels to cluster in the membrane and the evidence for specific interaction between PI and ETM suggest that the membrane might use alternative mechanisms to adapt to this long hydrophobic viroporin. These questions will be investigated in the future.

MATERIALS AND METHODS

Expression and purification of isotopically labeled ETM (8 to 38)

The ETM construct used in this study corresponds to residues 8 to 38 (⁸ETG TLIVN SVLLF LAFVV FLLVT LAILT ALR³⁸) of the SARS-CoV-2 E protein from the Wuhan-Hu-1 strain (National Center for Biotechnology Information reference YP_009724392.1). *E. coli* BL21 (DE3) cells were transformed with a Champion pET-SUMO plasmid encoding ETM fused to a His₆-SUMO tag at the N terminus. Cells were grown in M9 media at 37°C until an OD₆₀₀ (optical density at 600 nm) of 0.9. Then, His₆-SUMO-ETM expression was induced with 0.8 mM isopropyl-β-D-thiogalactopyranoside (IPTG) and proceeded for 16 hours overnight under shaking at 18°C. The cells were harvested and suspended in lysis buffer [50 mM tris (pH 8), 100 mM NaCl, and 1 mM MgSO₄] containing lysozyme (0.5 mg/ml), 1% Triton X-100, and 500 U of benzonase nuclease (Millipore). Lysis was carried out by sonication on ice, followed by removal of the cell debris by centrifugation at 20,000g.

The soluble fraction of the cell lysate was incubated with 2 ml of Ni²⁺ Profinity IMAC resin (Bio-Rad) per liter of M9 culture. Impurities were washed out with 30 mM imidazole, and His₆-SUMO-ETM was eluted with 250 mM imidazole in 50 mM tris buffer (pH 8, 100 mM NaCl and 0.1% *n*-dodecyl-β-D-maltoside). The His₆-SUMO-ETM fractions were diluted to ≤80 mM imidazole and treated with SUMO protease (0.5 mg/ml) and 2 mM tris(2-carboxyethyl)phosphine for 2 hours at 20°C with gentle rocking. The cleavage mixture was purified by reversed-phase high-performance liquid chromatography (HPLC) (Agilent 1290 Infinity II System) using an Agilent C3 column (21.2 mm × 150 mm, 5-μm particle size) with a linear 5 to 99% channel B gradient, at a flow rate of 10 ml/min at room temperature. Channel A is water with 0.1% trifluoroacetic acid (TFA), while channel B is 9:1 acetonitrile : isopropyl alcohol with 0.1% TFA. ETM was eluted at 40 min. The average yield of isotopically labeled ETM is 15 ± 2 mg/liter of M9 culture (28, 29).

The M9 media used to produce U-¹³C-labeled ETM used ¹³C₆-D-glucose (3 g/liter) and unlabeled ammonium chloride (1 g/liter). For ¹⁵N-labeled ETM, unlabeled glucose and ¹⁵N-labeled NH₄Cl were used in the M9 media. For doubly ¹³C,¹⁵N-labeled ETM (CN-ETM), ¹³C₆-D-glucose (3 g/liter) and ¹⁵NH₄Cl (1 g/liter) were added in the M9 media. For 1,3-¹³C-labeled ETM and 2-¹³C-labeled ETM, 1,3-¹³C-glycerol or 2-¹³C-glycerol (3 g/liter) was used as the carbon source instead of glucose.

The M9 media for CDN-ETM contained ¹³C₆-²H₇-D-glucose (3 g/liter), ¹⁵NH₄Cl (1 g/liter), and deuterium oxide (99%). Fractionally deuterated (FD) ¹⁵N-ETM (41) was expressed using unlabeled D-glucose (4 g/liter), ¹⁵NH₄Cl (1 g/liter), and deuterated water. This FD ¹⁵N-ETM was mixed with ¹³C-labeled ETM for the NHHC experiment to remove potential intramolecular ¹⁵N-¹³C cross peaks with natural abundance Ca and Cβ sites. Before protein expression

in deuterated media, cells were gradually adapted to deuterium at 37°C. First, cell colonies were transfected to 5 ml of LB dissolved in 50% deuterated water and incubated overnight. Second, cells were inoculated starting at an OD₆₀₀ of ~0.15 in 10 ml of unlabeled M9 dissolved in 90% deuterated water and incubated until an OD₆₀₀ of ~1. Third, cell cultures were scaled up to 150 ml of unlabeled M9 in 99% deuterated water and grown until an OD₆₀₀ of >2. Last, cells were harvested by gentle centrifugation (1000g) and resuspended in 1 liter of 99% ²H M9 containing the appropriate labeled sources to reach an initial OD₆₀₀ of 0.3. ETM expression was induced with 0.8 mM IPTG at an OD₆₀₀ of 0.9, and expression continued for 24 hours at 18°C with shaking.

Synthesis of 4-¹⁹F-Phe-labeled ETM peptides

Fluorinated ETM peptides were synthesized by Fmoc solid-phase chemistry using fluorinated 4-F-Phe and 4-CF₃-Phe (Chem-Impex). H-Rink amide ChemMatrix resin (0.050 mmol, 0.10 g at 0.5 mmol/g loading size) was loaded into the reactor at 70°C. Amino acids were dissolved in hexafluorophosphate azabenzotriazole tetramethyl uronium (HATU) solution [2.5 ml per residue, 0.38 M in *N,N'*-dimethylformamide (DMF), 9.5 eq]. *N,N*-Diisopropylethylamine (DIEA) was added (348 μl, 2.0 mmol, 20 eq) immediately before amino acids were coupled in 10-fold excess (1.0 mmol) for 45 s. To reduce single-residue deletion impurities, double coupling was performed at I13, V14, ¹⁸LLFL²¹, ²³FVVFL²⁸, and R38. Each residue was deprotected with 20% piperidine in DMF solution for 25 s. After the final coupling step, the resin was dried, and the peptide was deprotected and cleaved from the resin using 5 ml of TFA/phenol/water/triisopropylsilane (TIPS) solution (88:5:5:2, v/v) for 2 hours. The resin was filtered, and the crude peptide was precipitated using cold 1:1 (v/v) hexane:diethyl ether, washed, and dried at low pressure.

The crude peptide was dissolved in trifluoroethanol (TFE) and purified by reversed-phase HPLC using a Vydac C4 column (22 mm × 250 mm, 10-μm particle size) and a linear gradient of 80 to 100% methanol against 20 to 0% water over 25 min at a flow rate of 10 ml/min. ETM peptides were eluted at ~99% methanol (6). The combined yield of the synthesis and purification was ~2%.

Preparation of proteoliposome samples

Three lipid membrane compositions were prepared in this study (table S1). The ERGIC-mimetic lipid membrane consists of 45:20:13:7:15 molar ratios of POPC, 1-palmitoyl-2-oleoyl-*sn*-glycero-3-phosphoethanolamine, bovine liver PI, 1-palmitoyl-2-oleoyl-*sn*-glycero-3-phospho-L-serine, and cholesterol (30, 73). Deuterated lipids were used for ¹H-detected measurements, composed by a mixture of 1,2-dimyristoyl-*d*₅₄-*sn*-glycero-3-phosphocholine (DMPC-*d*₅₄) and 1,2-dimyristoyl-*d*₅₄-*sn*-glycero-3-[phospho-rac-(1-glycerol)] (DMPG-*d*₅₄) at a 7:3 molar ratio. The low viscosity lipid membranes consisted of a 7:3 mixture of POPC:POPG lipids.

The desired lipids (Avanti Polar Lipids) were dissolved in a 1:1 chloroform:methanol solution, while ETM was dissolved in TFE. When mixtures of differentially labeled ETM were required, the peptide solutions were mixed at a 1:1 molar ratio with sonication. The peptide solution was mixed with the lipid solution, the organic solvent was dried under a stream of nitrogen gas, and then the sample was lyophilized overnight. Proteoliposomes were formed by suspending the dry film in buffer under vigorous mixing and

then incubated for 60 min. The buffer consisted of 30 mM sodium acetate at pH 4.5, 30 mM CaCl₂, 10 mM NaCl, and 0.15 mM NaN₃. The proteoliposome mixture was then subjected to 10 freeze/thaw cycles between liquid nitrogen temperature and a 45°C water bath. Proteoliposomes were collected by ultracentrifugation at 250,000g using a Beckman SW60 Ti swinging-bucket rotor. The resulting membrane pellet was dried under a gentle stream of nitrogen until the hydration level reached ~40% (w/w) water to total mass. The membrane pellets were centrifuged into 3.2-, 1.9-, or 1.3-mm rotors for NMR experiments.

Proteoliposomes were prepared at a range of P/L molar ratio to achieve optimal performance of the NMR experiments. The P/L ratio is calculated as the ratio of protein monomer to total lipids, including cholesterol (table S1). High P/L ratios of 1:9 to 1:15 were used for 3D ¹H-detected resonance assignment experiments and N-C and C-C intermolecular distance measurements. Low P/L ratios of 1:20 to 1:40 were used for ¹H-¹⁹F, ¹³C-¹⁹F, and ¹⁹F-¹⁹F distance measurements and N-H dipolar coupling measurements to minimize channel clustering and to promote uniaxial rotational diffusion, respectively.

Solid-state NMR spectroscopy

Solid-state NMR experiments were conducted at 800, 900, and 600 MHz using Bruker Avance spectrometers (table S9). The 800-MHz (18.8 T) experiments were conducted using a BlackFox 3.2-mm HCN MAS probe. The 900-MHz (21.1 T) spectra were measured with a Bruker 3.2-mm Efree HCN probe. All ¹⁹F NMR spectra were measured on a 600-MHz (14.1 T) spectrometer using a Bruker 1.9-mm HFX probe. ¹H-detected spectra at 55-kHz MAS were measured at 600 and 800 MHz using Bruker 1.3-mm HCN probes. Most experiments were conducted between 273 and 287 K except when otherwise noted.

All ¹³C chemical shifts were externally referenced to the adamantane CH₂ chemical shift at 38.48 parts per million (ppm) on the TMS scale. ¹⁵N chemical shifts were referenced to the ¹⁵N peaks of the model tripeptide *N*-formyl-Met-Leu-Phe at 127.88, 118.57, and 110.09 ppm on the liquid ammonia scale. ¹⁹F chemical shifts were referenced to the ¹⁹F peak of 5-¹⁹F-tryptophan at -122.1 ppm on the CF₃Cl scale. ¹H chemical shifts were referenced internally to the POPC H_γ chemical shift at 3.264 ppm on the DSS scale. The reported sample temperatures were estimated from the ¹H chemical shift of bulk water using the equation $T_{\text{sample}} = (7.762 - \delta_{\text{water}}) \times 96.9 \text{ K}$ (74).

2D ¹⁵N-¹³C and ¹³C-¹³C correlation spectra were measured on the 800-MHz spectrometer under 10.5-kHz MAS and on the 900-MHz spectrometer under 11.8-kHz MAS. ¹⁵N-¹³C polarization transfer was achieved using the SPECIFIC-CP sequence (75) with a 6-ms contact time. Intermolecular NHC polarization transfer was achieved with 1-ms ¹H spin diffusion. 2D ¹³C-¹³C correlation spectra were measured using 25-, and 300-ms CORD mixing (76). Water-edited 2D CC correlation spectra were measured using a water-selective ¹H Hahn echo consisting of a 952-μs (i.e., 10 rotor periods) Gaussian 180° pulse and a pair of 95-μs delays. The total echo duration was therefore 1.14 ms (77). This ¹H T₂ filter was followed by a variable-length ¹H spin diffusion period to transfer the water ¹H polarization to the protein protons. Similarly, ¹H-detected water-edited 2D hNH spectra were measured under 55-kHz MAS using a water-selective Gaussian 180° pulse in the middle of a ¹H Hahn echo period of 3.5 ms. The average absolute uncertainty for

the water-edited *S/S*₀ intensities is ±0.03 for the 2D CC spectra and ±0.01 for the 2D hNH spectra. Lipid-edited 2D CC spectra were measured under 10.5-kHz MAS using a lipid-selective Gaussian 180° pulse in the middle of a Hahn echo period of 1.3 ms. The experiment was conducted at 310 K to achieve sufficient mobility for the lipid acyl chains so that the lipid ¹H magnetization can be preferentially selected over the protein ¹H signals.

The 2D ¹⁵N-¹H DIPSHIFT experiment (78, 79) was used to measure N-H dipolar couplings of ETM under fast uniaxial rotational diffusion to determine the helix orientation (34, 35). The N-H DIPSHIFT experiment was conducted under 7-kHz MAS using a dipolar-doubled version of the pulse sequence to increase the precision of the dipolar coupling measurement (80). ¹H homonuclear decoupling was achieved using the FSLG pulse sequence (81) with a transverse rf field strength of 83 kHz. To enhance site resolution, we further used the 2D ¹⁵N-¹³Ca correlation experiment as the readout for the N-H dipolar coupling. Two 2D NCa spectra without N-H dipolar dephasing (*S*₀) and with half a rotor period of dephasing (*S*) (82) were measured. Additional 2D ¹³C-¹H DIPSHIFT spectra were measured to confirm the rotational diffusion of the protein. All DIPSHIFT spectra were measured at a high sample temperature of 38°C to enable the ETM helical bundle to undergo uniaxial rotational diffusion. The sample was equilibrated at this temperature for at least 4 hours before the measurement.

¹H-detected 3D hCANH and hCA(CO)NH spectra were measured under 55-kHz MAS to assign the ¹H and ¹⁵N chemical shifts (83, 84). The hCANH spectrum was measured at 800 MHz to provide intra-residue correlations. The hCA(CO)NH spectrum was measured at 600 MHz to provide interresidue correlations for sequential assignment.

All ¹⁹F NMR experiments were conducted on the 600-MHz spectrometer. 1D ¹³C-¹⁹F REDOR experiments were conducted under 14-kHz MAS at 20°C. Ca-selective REDOR experiments used a 248-μs Gaussian 180° pulse centered at 64.2 ppm to selectively refocus the Ca signals. The 2D hNH-resolved ¹H-¹⁹F REDOR experiment (85) was conducted under 38-kHz MAS at ~10°C using 3.4-ms REDOR dephasing.

The ¹⁹F CODEX experiment (38) was conducted under 18-kHz MAS at a sample temperature of 244 K. This low temperature was chosen to ensure that no slow motion occurs during the CODEX mixing time so that only spin diffusion effects are measured (86). ¹H-¹⁹F CP was implemented using a spin-lock field strength of 77 kHz for ¹H and 59 kHz for ¹⁹F, following the sideband matching condition. The two rotor-synchronized π-pulse trains that recouple the ¹⁹F chemical shift anisotropy (CSA) were 0.11 ms each. The two π-pulse trains were separated by a mixing time (*t*_m) during which ¹H-driven ¹⁹F spin diffusion occurs. After the second π-pulse train, a *z*-filter (*t*_z) was used to correct for *T*₁ relaxation. The ¹H decoupling field strength during the ¹⁹F CSA recoupling periods was 120 kHz. The experiment was run in pairs: The control experiment (*S*₀) consists of a short (10 μs) *t*_m and a long *t*_z, while the exchange experiment (*S*) interchanges the lengths of *t*_z and *t*_m. The *S*₀ and *S* spectra were alternately measured in blocks 1.5 hours to minimize the effects of spectrometer drift.

NMR data analysis

All NMR spectra were processed in the TopSpin 3.2 software. Chemical shift assignment was conducted in NMRFAM-SPARKY 1.4. Typical processing used either QSINE apodization with SSB = 3

or Gaussian apodization with LB = -20 Hz and GB = 0.05. 2D correlation spectra were plotted with a scaling factor of 1.2 between successive contour lines. REDOR curve fittings were generated using Python scripts.

Hydration maps for water-edited 2D CC spectra were calculated using a Python script (77). Intensities of 4-, 9-, and 100-ms ^1H spin diffusion spectra were exported to the NMRglue package (87) and scaled by the number of scans. The intensities of the 4- and 9-ms spectra were divided pointwise by the 100-ms spectral intensities and plotted at contour levels between 0.00 and 0.50 in increments of 0.02. The spectra were noise-filtered by excluding $S/S_{100\text{ms}}$ ratios in which both S and S_0 intensities are lower than four times the noise level, which was estimated from a signal-free region of the spectra. The lipid-edited 2D CC and 2D NC-resolved N-H DIPSHIFT spectra were processed in the same manner, adjusted for the respective dynamic range.

^{13}C - ^{19}F and ^1H - ^{19}F REDOR curves were simulated using SIMPSON (88) as described before (89). REDOR curves were simulated for distances of 3.0 to 12.0 Å at 0.1-Å increments. Simulations accounted for ^{19}F pulse imperfection, ^{19}F CSA, and finite pulse length effects. Powder averaging was performed using the REPULSION320 scheme (90). Best-fit simulations were determined from the minimum RMSDs from the measured intensities. Simulated curves for distances 0.5 Å away from the best-fit value were also shown in the REDOR plots to represent the approximate uncertainty of the distance measurements.

The intermolecular ^{13}C - ^{19}F REDOR experiments were conducted on a 1:1 mixture of ^{13}C -labeled ETM and ^{19}F -labeled ETM. The probability that a ^{13}C -labeled protein is adjacent to a fluorinated protein is thus 50%. As a result, the simulated REDOR S/S_0 values were scaled by 0.5 using the equation $(S/S_0)_{\text{corr}} = 0.5 \times (S/S_0)_{\text{calc}} + 0.5$ to compare with the experimental intensities. The ^1H - ^{19}F REDOR experiments were similarly conducted on 1:1 mixtures of CDN-labeled protein and ^{19}F -labeled protein. However, ^1H - ^{19}F REDOR simulations required a larger scaling factor of 0.75 and correspondingly the equation $(S/S_0)_{\text{corr}} = 0.75 \times (S/S_0)_{\text{calc}} + 0.25$ to account for the statistics of intermolecular mixing. This choice is based on the empirical observation that the minimum measured ^1H - ^{19}F REDOR S/S_0 intensities are ~0.30 (fig. S10). This can be explained by the fact that the strong ^1H - ^{19}F dipolar coupling is sensitive to distances up to ~2 nm. Thus, a CDN-labeled peptide i has greater than 50% probability of being within ~2-nm radius of a fluorinated peptide, which may be at $i \pm 1$ or $i \pm 2$ positions in the pentamer. Because this scaling factor depends on the geometry of the specific H^N-F distance pair, we use a larger uncertainty of 2 Å for the ^1H - ^{19}F REDOR distance restraints.

The CODEX S/S_0 values were read off from the integrated intensity of the centerband and the upfield first-order sideband. The downfield first-order sideband was excluded because of partial overlap with the residual TFA peak at -75 ppm. Error bars σ on the S/S_0 values were estimated from the signal-to-noise ratio (SNR) of the spectra according to $\sigma = (S/S_0)[(\text{SNR}_{S_0}^{-2} + \text{SNR}_S^{-2})^{1/2}]$. Simulated CODEX curves were produced using matrix calculations based on the ^{19}F homonuclear dipolar coupling and ^1H -driven spin diffusion rates (6, 91). The single quantum overlap integral $F(0)$ was set to 3.4 μs (6). A five-spin system with the geometry of an ideal pentagon was used. The CODEX data were fit to this geometry by varying the nearest-neighbor ^{19}F - ^{19}F distance from 4 to 20 Å in increments of 0.1 Å while minimizing

$\chi_v^2 = \frac{1}{v} \sum (\text{exp} - \text{sim})^2 / \sigma^2$, where exp and sim are the experimental and simulated S/S_0 values, respectively, and v is the number of degrees of the freedom in the fit, which equals the number of data points minus one. The distance value giving the minimum χ_v^2 for is taken as the best-fit distance, while the distance range corresponds to distances for which $\chi_v^2 < \chi_{v,\text{min}}^2 + 1$.

Orientation-dependent N-H dipolar order parameters (S_{NH}) were obtained by fitting the measured ^{15}N - ^1H DIPSHIFT S/S_0 ratios, which were extracted from the intensity of each peak in the 2D ^{15}N - ^{13}C correlation spectra measured with half a rotor period of ^{15}N - ^1H dipolar dephasing [$S(t_r/2)$] and without dephasing (S_0). Only resolved peaks in the 2D spectra were used for the analysis. Uncertainties in the S/S_0 values were propagated from the SNRs of the peaks using the equation $\epsilon = (S/S_0)[(\text{SNR}_S^{-2} + \text{SNR}_{S_0}^{-2})^{1/2}]$. DIPSHIFT curves were simulated using a python script. The theoretical scaling factor of 0.577 was used for ^1H homonuclear decoupling with the FSLG sequence. The measured order parameters S_{NH} were scaled by 0.95 to match the theoretical rigid limit value of 10.5 kHz for a N-H bond at 7-kHz MAS.

The ^{15}N - ^1H dipolar wave was calculated as a function of the helix tilt angle (θ) relative to the membrane normal (z axis), assuming an ideal α helix with a periodicity of 3.6 residues per turn. Under uniaxial rotational diffusion about the bilayer normal, the N-H order parameter S_{NH} is

$$S_{\text{NH}} = \frac{3\cos^2\beta - 1}{2}$$

where $\cos\beta = \cos\theta\cos\psi + \sin\theta\sin\psi\cos\rho$ is the directional cosine between the N-H bond and the bilayer normal, which is the motional axis. ψ is the angle between the N-H bond and the α -helical axis, and ρ is the azimuthal angle of the N-H bond around the α -helical axis. For an ideal α helix, θ is constant, $\psi = 14.9^\circ$ (82), and $\rho = \rho_0 + 100^\circ \times n$, where n is the residue number.

XPLOR-NIH structure calculation

The low-pH and Ca^{2+} bound structure of ETM was calculated using the XPLOR-NIH software (45) hosted on the NMRbox server (92). The starting system was set with five extended ETM monomers (residues 8 to 38) placed in a perfect pentagon of radius 20 Å, with individual chains aligned parallel to the C_5 axis. After initial minimization in torsion angle space, each simulation began with 5000 steps of high-temperature torsion angle dynamics at 5000 K. This was followed by annealing from 5000 K to 20 K with a temperature decrements of 10 K and 100 steps of torsion angle dynamics at each temperature. Energy minimization was subsequently carried out first in torsion angle space and then in Cartesian coordinates. The experimental restraints (Table 1) include backbone torsion angles, N-H bond orientations, and intramolecular and intermolecular distance restraints (tables S3 to S7). Even without using short-range intramolecular restraints, we found that the (ϕ and ψ) torsion angles, orientational angles, NHHC, and CC distance restraints already led to largely converged structures. This means that the backbone conformation is well constrained by the dihedral and orientational angles, whereas the side-chain conformations are well constrained by intermolecular distances and the C_5 symmetry. The intermolecular C-F and H-F distance restraints further improved the structural resolution.

During the XPLOR-NIH simulations, the five ETM monomers were restrained to be identical using the noncrystallographic symmetry term PosDiffPot and the translational symmetry term DistSymmPot. The symmetry restraints were lifted for residues Phe²⁰ and Phe²⁶ because their side chains had been shown before to adopt two different rotameric states (29). Hydrogen bonds were included using the HBPot term (93). Standard bond angles and bond lengths were set with terms BOND, ANGL, and IMPR, and the nonbonded potential was implemented with XPLOR's VDW term. The exact parameters used in all energy potentials are listed in table S8. Four types of experimental restraints were used for structure calculation: chemical shift-derived backbone (ϕ and ψ) torsion angles, N-H dipolar couplings, intramolecular contacts (NOEs), and intermolecular NOEs.

Torsion angles (ϕ and ψ) were derived from ¹H, ¹⁵N, and ¹³C chemical shifts using TALOS-N predictions (94). These were implemented as the dihedral-angle restraint term CDIH. The N-H dipolar couplings were implemented in units of hertz instead of kilohertz using the XPLOR residual dipolar coupling term RDC (table S3). Here, the magnitude of the alignment tensor (Da) was set to 10.5 Hz, and the rhombicity of the alignment tensor was set to 0 due to uniaxial rotation. Experimental dipolar couplings were converted to RDC dipolar splittings by multiplying by 2 and replacing kilohertz with hertz. Distance restraints (tables S4 to S6) were defined via the XPLOR nuclear Overhauser effect term NOE, which were set to soft. Each restraint was repeated five times, i.e., one set of restraints for each monomer.

All intermolecular contacts were ambiguously defined between chain i to the neighboring chain $i + 1$ or $i - 1$, but not to the chains across the pentamer. The intermolecular ¹³C-¹⁹F REDOR distance restraints were implemented as contacts between the H_α atom of Phe²⁰ (corresponding to para-¹⁹F in the sample) and carbon atoms of the $i + 1$ or $i - 1$ chain. The REDOR distance uncertainty was set to -1 Å for the lower bound and $+1.5$ Å for the upper bound to account for the uncertainty associated with the statistics of intermolecular mixing. Because Phe²⁰ adopts two states within each pentamer, the Phe²⁰ H-F or C-F distance restraints may not be satisfied by every one of the five Phe²⁰. Therefore, it would be improper to impose a given Phe²⁰ H-F or C-F distance on all five chains at the same time. Instead, we combined the contributions of all five monomers into single Phe²⁰-associated REDOR distance restraints, by calculating a given structure's REDOR NOE distance R from the 10 R_{ij} according to

$$R = \left[\sum_{F_i, C_{\alpha_j}} \left(\frac{R_{ij}^{-3}}{5} \right) \right]^{-\frac{1}{3}}$$

Using the measured Ala²² C α -Phe²⁰ F_z distance as an example, this R averaging matches the experimental measurement in the following way. The measured REDOR $\Delta S/S_0$ value reports the average dipolar dephasing of the five Ala²² C α to the fluorinated Phe²⁰. This average dipolar dephasing is proportional to $\sum_{F_i, C_{\alpha_j}} \left(\frac{R_{ij}^{-3}}{5} \right)$. To compare this average distance with the measured two-spin REDOR distance, we take the $(-1/3)$ power of this average. For all contacts not involving Phe side chains, distance averaging was defined as $(\sum_{i,j} R_{ij}^{-6})^{-\frac{1}{6}}$, which is the standard approach for evaluating spin diffusion or NOE cross peaks in 2D and 3D correlation spectra.

Intramolecular ¹³C-¹³C distance restraints were implemented as NOE restraints with an upper limit of 8 Å for correlations observed in the 300-ms spectra. Intermolecular ¹³C-¹³C distance restraints were set with an upper limit of 10 Å for the 300-ms spectra. Cross peaks in the 2D NHC spectra with 1-ms ¹H spin diffusion were given a distance upper bound of 8.5 Å.

Calculated ETM structures were sorted by total energy. The final production run included 3000 independent simulations. Of these, we selected the 30 lowest-energy structural models for the final ensemble. Calculations using 1000 simulations did not give sufficiently converged result, with the 100 lowest-energy models still showing many violations. With 2000 simulations, the number of violations and the total energies decreased among the 100 lowest-energy models. With 3000 simulations, the number of violations and the total energies are both low for the 100 lowest-energy models.

The channel pore diameter profile is based on the van der Waals radius generated using the HOLE software (95) on the lowest-energy structures. The HOLE spherical probe radius was set to 6 Å. The structural models were visualized in PyMOL v2.3.4.

Supplementary Materials

This PDF file includes:

Figs. S1 to S11

Tables S1 to S9

REFERENCES AND NOTES

1. E. de Wit, N. van Doremalen, D. Falzarano, V. J. Munster, SARS and MERS: Recent insights into emerging coronaviruses. *Nat. Rev. Microbiol.* **14**, 523–534 (2016).
2. A. Zumla, J. F. Chan, E. I. Azhar, D. S. Hui, K.-Y. Yuen, Coronaviruses—Drug discovery and therapeutic options. *Nat. Rev. Drug Discov.* **15**, 327–347 (2016).
3. J. Piret, G. Boivin, Pandemics throughout history. *Front. Microbiol.* **11**, 631736 (2020).
4. D. Schoeman, B. C. Fielding, Coronavirus envelope protein: Current knowledge. *Virus* **16**, 69 (2019).
5. L. Mendonça, A. Howe, J. B. Gilchrist, Y. Sheng, D. Sun, M. L. Knight, L. C. Zanetti-Domingues, B. Bateman, A. S. Krebs, L. Chen, J. Radecke, V. D. Li, T. Ni, I. Kounatidis, M. A. Koronfel, M. Szykiewicz, M. Harkiolaki, M. L. Martin-Fernandez, W. James, P. Zhang, Correlative multi-scale cryo-imaging unveils SARS-CoV-2 assembly and egress. *Nat. Commun.* **12**, 4629 (2021).
6. N. H. Somberg, W. W. Wu, J. Medeiros-Silva, A. J. Dregni, H. Jo, W. F. DeGrado, M. Hong, SARS-CoV-2 envelope protein forms clustered pentamers in lipid bilayers. *Biochemistry* **61**, 2280–2294 (2022).
7. P. Venkatagopalan, S. M. Daskalova, L. A. Lopez, K. A. Dolezal, B. G. Hogue, Coronavirus envelope (E) protein remains at the site of assembly. *Virology* **478**, 75–85 (2015).
8. J. L. Nieto-Torres, M. L. DeDiego, C. Verdía-Baguena, J. M. Jimenez-Guardeno, J. A. Regla-Nava, R. Fernandez-Delgado, C. Castano-Rodriguez, A. Alcaraz, J. Torres, V. M. Aguilera, L. Enjuanes, Severe acute respiratory syndrome coronavirus envelope protein ion channel activity promotes virus fitness and pathogenesis. *PLOS Pathog.* **10**, e1004077 (2014).
9. U. Breiting, N. S. Farag, H. Sticht, H.-G. Breiting, Viroporins: Structure, function, and their role in the life cycle of SARS-CoV-2. *Int. J. Biochem. Cell Biol.* **145**, 106185 (2022).
10. A. Mehregan, S. Perez-Conesa, Y. Zhuang, A. Elbahsi, D. Pasini, E. Lindahl, R. J. Howard, C. Ulens, L. Delemotte, Probing effects of the SARS-CoV-2 E protein on membrane curvature and intracellular calcium. *Biochim. Biophys. Acta. Biomembr.* **1864**, 183994 (2022).
11. A. J. Dregni, M. J. McKay, W. Surya, M. Queralto-Martin, J. Medeiros-Silva, H. K. Wang, V. Aguilera, J. Torres, M. Hong, The cytoplasmic domain of the SARS-CoV-2 envelope protein assembles into a β -sheet bundle in lipid bilayers. *J. Mol. Biol.* **435**, 167966 (2023).
12. J. Chai, Y. Cai, C. Pang, L. Wang, S. McSweeney, J. Shanklin, Q. Liu, Structural basis for SARS-CoV-2 envelope protein recognition of human cell junction protein PALS1. *Nat. Commun.* **12**, 3433 (2021).
13. M. Zheng, R. Karki, E. P. Williams, D. Yang, E. Fitzpatrick, P. Vogel, C. B. Jonsson, T. D. Kanneganti, TLR2 senses the SARS-CoV-2 envelope protein to produce inflammatory cytokines. *Nat. Immunol.* **22**, 829–838 (2021).
14. J. M. Jimenez-Guardeno, J. L. Nieto-Torres, M. L. DeDiego, J. A. Regla-Nava, R. Fernandez-Delgado, C. Castano-Rodriguez, L. Enjuanes, The PDZ-binding motif of severe acute

- respiratory syndrome coronavirus envelope protein is a determinant of viral pathogenesis. *PLOS Pathog.* **10**, e1004320 (2014).
15. K. R. Vann, A. Acharya, S. M. Jang, C. Lachance, M. Zandian, T. A. Holt, A. L. Smith, K. Pandey, D. L. Durden, D. El-Gamal, J. Côté, S. N. Byrreddy, T. G. Kutateladze, Binding of the SARS-CoV-2 envelope E protein to human BRD4 is essential for infection. *Structure* **30**, 1224–1232.e5 (2022).
 16. B. Xia, X. Shen, Y. He, X. Pan, F. L. Liu, Y. Wang, F. Yang, S. Fang, Y. Wu, Z. Duan, X. Zuo, Z. Xie, X. Jiang, L. Xu, H. Chi, S. Li, Q. Meng, H. Zhou, Y. Zhou, X. Cheng, X. Xin, L. Jin, H. L. Zhang, D. D. Yu, M. H. Li, X. L. Feng, J. Chen, H. Jiang, G. Xiao, Y. T. Zheng, L. K. Zhang, J. Shen, J. Li, Z. Gao, SARS-CoV-2 envelope protein causes acute respiratory distress syndrome (ARDS)-like pathological damages and constitutes an antiviral target. *Cell Res.* **31**, 847–860 (2021).
 17. J. L. Nieto-Torres, C. Verdía-Baguena, J. M. Jimenez-Guardeno, J. A. Regla-Nava, C. Castano-Rodriguez, R. Fernandez-Delgado, J. Torres, V. M. Aguilera, L. Enjuanes, Severe acute respiratory syndrome coronavirus E protein transports calcium ions and activates the NLRP3 inflammasome. *Virology* **485**, 330–339 (2015).
 18. M. L. DeDiego, E. Alvarez, F. Almazan, M. T. Rejas, E. Lamirande, A. Roberts, W. J. Shieh, S. R. Zaki, K. Subbarao, L. Enjuanes, A severe acute respiratory syndrome coronavirus that lacks the E gene is attenuated in vitro and in vivo. *J. Virol.* **81**, 1701–1713 (2007).
 19. B. Bosen, V. Legros, B. Zhou, E. Siret, C. Mathieu, F. L. Cosset, D. Lavillette, S. Denolly, The SARS-CoV-2 envelope and membrane proteins modulate maturation and retention of the spike protein, allowing assembly of virus-like particles. *J. Biol. Chem.* **296**, 100111 (2021).
 20. A. Santamaria, K. C. Batchu, O. Matsarskaia, S. F. Prevost, D. Russo, F. Natali, T. Seydel, I. Hoffmann, V. Laux, M. Haertlein, T. A. Darwish, R. A. Russell, G. Corucci, G. Fragneto, A. Maestro, N. R. Zaccai, Strikingly different roles of SARS-CoV-2 fusion peptides uncovered by neutron scattering. *J. Am. Chem. Soc.* **144**, 2968–2979 (2022).
 21. K. Takeuchi, R. A. Lamb, Influenza virus M2 protein ion channel activity stabilizes the native form of fowl plague virus hemagglutinin during intracellular transport. *J. Virol.* **68**, 911–919 (1994).
 22. J. W. Westerbeck, C. E. Machamer, The infectious bronchitis coronavirus Envelope protein alters Golgi pH to protect the spike protein and promote the release of infectious virus. *J. Virol.* **93**, e00015–e00019 (2019).
 23. U. Breitingner, N. K. M. Ali, H. Sticht, H.-G. Breitingner, Inhibition of SARS CoV envelope protein by flavonoids and classical viroporin inhibitors. *Front. Microbiol.* **12**, 692423 (2021).
 24. J. Torres, K. Parthasarathy, X. Lin, R. Saravanan, A. Kukol, D. X. Liu, Model of a putative pore: The pentameric α -helical bundle of SARS coronavirus E protein in lipid bilayers. *Biophys. J.* **91**, 938–947 (2006).
 25. K. Pervushin, E. Tan, K. Parthasarathy, X. Lin, F. L. Jiang, D. Yu, A. Vararattanavech, T. W. Soong, D. X. Liu, J. Torres, Structure and inhibition of the SARS coronavirus envelope protein ion channel. *PLOS Pathog.* **5**, e1000511 (2009).
 26. W. Surya, Y. Li, J. Torres, Structural model of the SARS coronavirus E channel in LMPG micelles. *Biochim. Biophys. Acta. Biomembr.* **1860**, 1309–1317 (2018).
 27. B. Reif, S. E. Ashbrook, L. Emsley, M. Hong, Solid-state NMR spectroscopy. *Nat. Rev. Methods Primers* **1**, 2 (2021).
 28. V. S. Mandala, M. J. McKay, A. A. Shcherbakov, A. J. Dregni, A. Kolocouris, M. Hong, Structure and drug binding of the SARS-CoV-2 envelope protein transmembrane domain in lipid bilayers. *Nat. Struct. Mol. Biol.* **27**, 1202–1208 (2020).
 29. J. Medeiros-Silva, N. H. Somberg, H. K. Wang, M. J. McKay, V. S. Mandala, A. J. Dregni, M. Hong, PH- and calcium-dependent aromatic network in the SARS-CoV-2 envelope protein. *J. Am. Chem. Soc.* **144**, 6839–6850 (2022).
 30. A. Schweizer, H. Clausen, G. van Meer, H. P. Hauri, Localization of O-glycan initiation, sphingomyelin synthesis, and glucosylceramide synthesis in Vero cells with respect to the endoplasmic reticulum-Golgi intermediate compartment. *J. Biol. Chem.* **269**, 4035–4041 (1994).
 31. Y. Zhou, T. K. Frey, J. J. Yang, Viral calciomics: Interplays between Ca^{2+} and virus. *Cell Calcium* **46**, 1–17 (2009).
 32. J. Sargeant, J. C. Hay, Ca^{2+} regulation of constitutive vesicle trafficking. *Fac. Rev.* **11**, 6 (2022).
 33. J. Torres, U. Maheswari, K. Parthasarathy, L. Ng, D. X. Liu, X. Gong, Conductance and amantadine binding of a pore formed by a lysine-flanked transmembrane domain of SARS coronavirus envelope protein. *Protein Sci.* **16**, 2065–2071 (2007).
 34. S. D. Cady, C. Goodman, C. Tatko, W. F. DeGrado, M. Hong, Determining the orientation of uniaxially rotating membrane proteins using unoriented samples: A ^2H , ^{13}C , and ^{15}N solid-state NMR investigation of the dynamics and orientation of a transmembrane helical bundle. *J. Am. Chem. Soc.* **129**, 5719–5729 (2007).
 35. M. Hong, T. Doherty, Orientation determination of membrane-disruptive proteins using powder samples and rotational diffusion: A simple solid-state NMR approach. *Chem. Phys. Lett.* **432**, 296–300 (2006).
 36. S. H. Park, A. A. Mrse, A. A. Nevzorov, M. F. Mesleh, M. Oblatt-Montal, M. Montal, S. J. Opella, Three-dimensional structure of the channel-forming trans-membrane domain of virus protein “u” (Vpu) from HIV-1. *J. Mol. Biol.* **333**, 409–424 (2003).
 37. D. J. Barlow, J. M. Thornton, Helix geometry in proteins. *J. Mol. Biol.* **201**, 601–619 (1988).
 38. E. R. de Azevedo, T. J. Bonagamba, W. Hu, K. Schmidt-Rohr, Centerband-only detection of exchange: Efficient analysis of dynamics in solids by NMR. *J. Am. Chem. Soc.* **121**, 8411–8412 (1999).
 39. M. Hong, Determination of multiple ϕ -torsion angles in proteins by selective and extensive ^{13}C labeling and two-dimensional solid-state NMR. *J. Magn. Reson.* **139**, 389–401 (1999).
 40. V. A. Higman, J. Flinders, M. Hiller, S. Jehle, S. Markovic, S. Fiedler, B. J. van Rossum, H. Oschkinat, Assigning large proteins in the solid state: A MAS NMR resonance assignment strategy using selectively and extensively ^{13}C -labelled proteins. *J. Biomol. NMR* **44**, 245–260 (2009).
 41. D. Mance, T. Sinnige, M. Kaplan, S. Narasimhan, M. Daniels, K. Houben, M. Baldus, M. Weingarth, An efficient labelling approach to harness backbone and side-chain protons in ^1H -detected solid-state NMR spectroscopy. *Angew. Chem. Int. Ed. Engl.* **54**, 15799–15803 (2015).
 42. M. Roos, T. Wang, A. A. Shcherbakov, M. Hong, Fast magic-angle-spinning ^{19}F spin exchange NMR for determining nanometer ^{19}F – ^{19}F distances in proteins and pharmaceutical compounds. *J. Phys. Chem. B* **122**, 2900–2911 (2018).
 43. A. A. Shcherbakov, J. Medeiros-Silva, N. Tran, M. D. Gelenter, M. Hong, From angstroms to nanometers: Measuring interatomic distances by solid-state NMR. *Chem. Rev.* **122**, 9848–9879 (2022).
 44. A. A. Shcherbakov, G. Hisao, V. S. Mandala, N. E. Thomas, M. Soltani, E. A. Salter, J. H. Davis Jr., K. A. Henzler-Wildman, M. Hong, Structure and dynamics of the drug-bound bacterial transporter EmrE in lipid bilayers. *Nat. Commun.* **12**, 172 (2021).
 45. C. D. Schwieters, J. J. Kuszewski, N. Tjandra, G. M. Clore, The Xplor-NIH NMR molecular structure determination package. *J. Magn. Reson.* **160**, 65–73 (2003).
 46. A. J. Li, R. Nussinov, A set of van der Waals and coulombic radii of protein atoms for molecular and solvent-accessible surface calculation, packing evaluation, and docking. *Proteins* **32**, 111–127 (1998).
 47. S. Ghosh, T. A. Dellibovi-Ragheb, A. Kerviel, E. Pak, Q. Qiu, M. Fisher, P. M. Takvorian, C. Bleck, V. W. Hsu, A. R. Fehr, S. Perlman, S. R. Achar, M. R. Straus, G. R. Whittaker, C. A. M. de Haan, J. Kehrl, G. Altan-Bonnet, N. Altan-Bonnet, β -Coronaviruses use lysosomes for egress instead of the biosynthetic secretory pathway. *Cell* **183**, 1520–1535.e14 (2020).
 48. P. Paroutis, N. Touret, S. Grinstein, The pH of the secretory pathway: Measurement, determinants, and regulation. *Physiology* **19**, 207–215 (2004).
 49. J. Torres, J. Wang, K. Parthasarathy, D. X. Liu, The transmembrane oligomers of coronavirus protein E. *Biophys. J.* **88**, 1283–1290 (2005).
 50. Y. Li, W. Surya, S. Claudine, J. Torres, Structure of a conserved Golgi complex-targeting signal in coronavirus envelope proteins. *J. Biol. Chem.* **289**, 12535–12549 (2014).
 51. A. J. Scott, A. Niitsu, H. T. Kratochvil, E. J. M. Lang, J. T. Sengel, W. M. Dawson, K. R. Mahendran, M. Mravic, A. R. Thomson, R. L. Brady, L. Liu, A. J. Mulholland, H. Bayley, W. F. DeGrado, M. I. Wallace, D. N. Woolfson, Constructing ion channels from water-soluble α -helical barrels. *Nat. Chem.* **13**, 643–650 (2021).
 52. A. Acharya, V. Carnevale, G. Fiorin, B. G. Levine, A. Polishchuk, V. Balannick, I. Samish, R. A. Lamb, L. H. Pinto, W. F. DeGrado, M. L. Klein, Structure and mechanism of proton transport through the transmembrane tetrameric M2 protein bundle of the influenza A virus. *Proc. Natl. Acad. Sci. U.S.A.* **107**, 15075–15080 (2010).
 53. E. Khurana, M. Dal Peraro, R. DeVane, S. Vemparala, W. F. DeGrado, M. L. Klein, Molecular dynamics calculations suggest a conduction mechanism for the M2 proton channel from influenza A virus. *Proc. Natl. Acad. Sci. U.S.A.* **106**, 1069–1074 (2009).
 54. V. S. Mandala, M. D. Gelenter, M. Hong, Transport-relevant protein conformational dynamics and water dynamics on multiple time scales in an archetypal proton channel: Insights from solid-state NMR. *J. Am. Chem. Soc.* **140**, 1514–1524 (2018).
 55. C. M. Ives, N. J. Thomson, U. Zachariae, A cooperative knock-on mechanism underpins Ca^{2+} -selective cation permeation in TRPV channels. *J. Gen. Physiol.* **155**, e202213226 (2023).
 56. K. Saotome, A. K. Singh, M. V. Yelshanskaya, A. I. Sobolevsky, Crystal structure of the epithelial calcium channel TRPV6. *Nature* **534**, 506–511 (2016).
 57. B. Xia, Y. Wang, X. Pan, X. Cheng, H. Ji, X. Zuo, H. Jiang, J. Li, Z. Gao, Why is the SARS-CoV-2 Omicron variant milder? *Innovation* **3**, 100251 (2022).
 58. X. Hou, L. Pediti, M. M. Diver, S. B. Long, Crystal structure of the calcium release-activated calcium channel Orai. *Science* **338**, 1308–1313 (2012).
 59. L. Tang, T. M. Gamal El-Din, J. Payandeh, G. Q. Martinez, T. M. Heard, T. Scheuer, N. Zheng, W. A. Catterall, Structural basis for Ca^{2+} selectivity of a voltage-gated calcium channel. *Nature* **505**, 56–61 (2014).
 60. E. A. Morrison, A. E. Robinson, Y. Liu, K. A. Henzler-Wildman, Asymmetric protonation of EmrE. *J. Gen. Physiol.* **146**, 445–461 (2015).

61. L. Feng, E. B. Campbell, R. MacKinnon, Molecular mechanism of proton transport in CLC Cl^-/H^+ exchange transporters. *Proc. Natl. Acad. Sci. U.S.A.* **109**, 11699–11704 (2012).
62. V. Kane Dickson, L. Pedi, S. B. Long, Structure and insights into the function of a Ca^{2+} -activated Cl^- channel. *Nature* **516**, 213–218 (2014).
63. F. Zhu, G. Hummer, Pore opening and closing of a pentameric ligand-gated ion channel. *Proc. Natl. Acad. Sci. U.S.A.* **107**, 19814–19819 (2010).
64. P. Aryal, M. S. Sansom, S. J. Tucker, Hydrophobic gating in ion channels. *J. Mol. Biol.* **427**, 121–130 (2015).
65. S. Rao, G. Klesse, P. J. Stansfeld, S. J. Tucker, M. S. P. Sansom, A heuristic derived from analysis of the ion channel structural proteome permits the rapid identification of hydrophobic gates. *Proc. Natl. Acad. Sci. U.S.A.* **116**, 13989–13995 (2019).
66. Z. Jia, M. Yazdani, G. Zhang, J. Cui, J. Chen, Hydrophobic gating in BK channels. *Nat. Commun.* **9**, 3408 (2018).
67. M. A. Kasimova, A. Yazici, Y. Yudin, D. Granata, M. L. Klein, T. Rohacs, V. Carnevale, Ion channel sensing: Are fluctuations the crux of the matter? *J. Phys. Chem. Lett.* **9**, 1260–1264 (2018).
68. H. T. Kratochvil, L. C. Watkins, M. Mravic, J. L. Thomaston, J. M. Nicoludis, N. H. Somberg, L. Liu, M. Hong, G. A. Voth, W. F. DeGrado, Transient water wires mediate selective proton transport in designed channel proteins. *Nat. Chem.* **15**, 1012–1021 (2023).
69. C. Xu, P. Lu, T. M. Gamal El-Din, X. Y. Pei, M. C. Johnson, A. Uyeda, M. J. Bick, Q. Xu, D. Jiang, H. Bai, G. Reggiano, Y. Hsia, T. J. Brunette, J. Dou, D. Ma, E. M. Lynch, S. E. Boyken, P. S. Huang, L. Stewart, F. DiMaio, J. M. Kollman, B. F. Luisi, T. Matsuura, W. A. Catterall, D. Baker, Computational design of transmembrane pores. *Nature* **585**, 129–134 (2020).
70. G. G. Rhys, C. W. Wood, E. J. M. Lang, A. J. Mulholland, R. L. Brady, A. R. Thomson, D. N. Woolfson, Maintaining and breaking symmetry in homomeric coiled-coil assemblies. *Nat. Commun.* **9**, 4132 (2018).
71. M. Mravic, J. L. Thomaston, M. Tucker, P. E. Solomon, L. Liu, W. F. DeGrado, Packing of apolar side chains enables accurate design of highly stable membrane proteins. *Science* **363**, 1418–1423 (2019).
72. B. H. Falkenburger, J. B. Jensen, E. J. Dickson, B. C. Suh, B. Hille, Phosphoinositides: Lipid regulators of membrane proteins. *J. Physiol.* **588**, 3179–3185 (2010).
73. G. van Meer, D. R. Voelker, G. W. Feigenson, Membrane lipids: Where they are and how they behave. *Nat. Rev. Mol. Cell Biol.* **9**, 112–124 (2008).
74. A. Bockmann, C. Gardienet, R. Verel, A. Hunkeler, A. Loquet, G. Pintacuda, L. Emsley, B. H. Meier, A. Lesage, Characterization of different water pools in solid-state NMR protein samples. *J. Biomol. NMR* **45**, 319–327 (2009).
75. M. Baldus, A. T. Petkova, J. Herzfeld, R. G. Griffin, Cross polarization in the tilted frame: Assignment and spectral simplification in heteronuclear spin systems. *Mol. Phys.* **95**, 1197–1207 (1998).
76. G. Hou, S. Yan, J. Trebosc, J. P. Amoureux, T. Polenova, Broadband homonuclear correlation spectroscopy driven by combined R_2^2 sequences under fast magic angle spinning for NMR structural analysis of organic and biological solids. *J. Magn. Reson.* **232**, 18–30 (2013).
77. A. J. Dregni, P. Duan, M. Hong, Hydration and dynamics of full-length tau amyloid fibrils investigated by solid-state nuclear magnetic resonance. *Biochemistry* **59**, 2237–2248 (2020).
78. M. G. Munowitz, R. G. Griffin, G. Bodenhausen, T. H. Huang, Two-dimensional rotational spin-echo nuclear magnetic resonance in solids: Correlation of chemical shift and dipolar interactions. *J. Am. Chem. Soc.* **103**, 2529–2533 (2002).
79. M. Hong, J. D. Gross, R. G. Griffin, Site-resolved determination of peptide torsion angle ϕ from the relative orientations of backbone N–H and C–H bonds by solid-state NMR. *J. Phys. Chem. B* **101**, 5869–5874 (1997).
80. M. Hong, J. D. Gross, C. M. Rienstra, R. G. Griffin, K. K. Kumashiro, K. Schmidt-Rohr, Coupling amplification in 2D MAS NMR and its application to torsion angle determination in peptides. *J. Magn. Reson.* **129**, 85–92 (1997).
81. A. Bielecki, A. C. Kolbert, H. J. M. de Groot, R. G. Griffin, M. H. Levitt, Frequency-switched Lee-Goldburg sequences in solids. *Adv. Magn. Reson.* **14**, 111–124 (1990).
82. V. S. Mandala, A. R. Loftis, A. A. Shcherbakov, B. L. Pentelute, M. Hong, Atomic structures of closed and open influenza B M2 proton channel reveal the conduction mechanism. *Nat. Struct. Mol. Biol.* **27**, 160–167 (2020).
83. E. Barbet-Massin, A. J. Pell, J. S. Retel, L. B. Andreas, K. Jaudzems, W. T. Franks, A. J. Nieuwkoop, M. Hiller, V. Higan, P. Guerry, A. Bertarello, M. J. Knight, M. Felletti, T. Le Marchand, S. Kotelovica, I. Akopjana, K. Tars, M. Stoppini, V. Bellotti, M. Bolognesi, S. Ricagno, J. J. Chou, R. G. Griffin, H. Oschkinat, A. Lesage, L. Emsley, T. Herrmann, G. Pintacuda, Rapid proton-detected NMR assignment for proteins with fast magic angle spinning. *J. Am. Chem. Soc.* **136**, 12489–12497 (2014).
84. D. H. Zhou, G. Shah, M. Cormos, C. Mullen, D. Sandoz, C. M. Rienstra, Proton-detected solid-state NMR spectroscopy of fully protonated proteins at 40 kHz magic-angle spinning. *J. Am. Chem. Soc.* **129**, 11791–11801 (2007).
85. A. A. Shcherbakov, V. S. Mandala, M. Hong, High-sensitivity detection of nanometer ^1H - ^{19}F distances for protein structure determination by ^1H -detected fast MAS NMR. *J. Phys. Chem. B* **123**, 4387–4391 (2019).
86. J. J. Buffry, A. J. Waring, M. Hong, Determination of peptide oligomerization in lipid bilayers using ^{19}F spin diffusion NMR. *J. Am. Chem. Soc.* **127**, 4477–4483 (2005).
87. J. J. Helmus, C. P. Jaroniec, NmrGlue: An open source Python package for the analysis of multidimensional NMR data. *J. Biomol. NMR* **55**, 355–367 (2013).
88. M. Bak, J. T. Rasmussen, N. C. Nielsen, SIMPSON: A general simulation program for solid-state NMR spectroscopy. *J. Magn. Reson.* **147**, 296–330 (2000).
89. A. A. Shcherbakov, M. Hong, Rapid measurement of long-range distances in proteins by multidimensional ^{13}C - ^{19}F REDOR NMR under fast magic-angle spinning. *J. Biomol. NMR* **71**, 31–43 (2018).
90. M. Bak, N. C. Nielsen, REPULSION, a novel approach to efficient powder averaging in solid-state NMR. *J. Magn. Reson.* **125**, 132–139 (1997).
91. W. Luo, M. Hong, Determination of the oligomeric number and intermolecular distances of membrane protein assemblies by anisotropic ^1H -driven spin diffusion NMR spectroscopy. *J. Am. Chem. Soc.* **128**, 7242–7251 (2006).
92. M. W. Maciejewski, A. D. Schuyler, M. R. Gryk, I. I. Moraru, P. R. Romero, E. L. Ulrich, H. R. Eghbalnia, M. Livny, F. Delaglio, J. C. Hoch, NMRBox: A resource for biomolecular NMR computation. *Biophys. J.* **112**, 1529–1534 (2017).
93. C. D. Schwieters, G. A. Bermejo, G. M. Clore, A three-dimensional potential of mean force to improve backbone and sidechain hydrogen bond geometry in Xplor-NIH protein structure determination. *Protein Sci.* **29**, 100–110 (2020).
94. Y. Shen, A. Bax, Protein backbone and sidechain torsion angles predicted from NMR chemical shifts using artificial neural networks. *J. Biomol. NMR* **56**, 227–241 (2013).
95. O. S. Smart, J. G. Neduvellil, X. Wang, B. A. Wallace, M. S. Sansom, HOLE: A program for the analysis of the pore dimensions of ion channel structural models. *J. Mol. Graph.* **14**, 354–360 (1996).

Acknowledgments

Funding: This work was supported by NIH grant GM088204 to M.H. J.M.-S. acknowledges Rubicon Fellowship 452020132 supported by the Netherlands Organization for Health Research and Development (ZonMw) and EMBO for supporting a Non-Stipendiary Postdoctoral Fellowship ALTF 1056-2020. N.H.S. acknowledges support by an NSF fellowship 1745302. The experiments here made use of NMR spectrometers at the Massachusetts Institute of Technology/Harvard Center for Magnetic Resonance, supported by NIH grant P41 GM132079. Structure calculation made use of the NMRbox, supported by NIH grant P41 GM111135. **Author contributions:** J.M.-S. expressed and purified the protein. N.H.S. synthesized the fluorinated peptides. J.M.-S. and N.H.S. conducted solid-state NMR experiments with help from A.J.D. and P.D. J.M.-S., N.H.S., A.J.D., and P.D. analyzed the data. J.M.-S. and A.J.D. calculated the structure. M.H. designed the project and supervised the experiments and data analysis. All authors discussed the results of the study. J.M.-S. and M.H. wrote the paper with contributions from the other authors. **Competing interests:** The authors declare that they have no competing interests. **Data and materials availability:** All NMR chemical shifts, distance, and torsion angle restraints have been deposited in the Biological Magnetic Resonance Bank (BMRB) with ID number 51946. The structural coordinates for the open-state ETM have been deposited in the Protein Data Bank with the accession code 8SUZ. All data needed to evaluate the conclusions in the paper are present in the paper and/or the Supplementary Materials.

Submitted 24 May 2023

Accepted 8 September 2023

Published 13 October 2023

10.1126/sciadv.adi9007